

Spatially selective activation of the visual cortex via intraneural stimulation of the optic nerve

Vivien Gaillet^{1,4}, Annarita Cutrone^{2,4}, Fiorenzo Artoni^{1,2,3,4}, Paola Vagni¹, Ariastity Mega Pratiwi¹, Sandra Alejandra Romero¹, Dario Lipucci Di Paola², Silvestro Micera^{2,3,5} and Diego Ghezzi^{1,5*}

Retinal prostheses can restore a functional form of vision in patients affected by dystrophies of the outer retinal layer. Beyond clinical utility, prostheses for the stimulation of the optic nerve, the visual thalamus or the visual cortex could also serve as tools for studying the visual system. Optic-nerve stimulation is particularly promising because it directly activates nerve fibres, takes advantage of the high-level information processing occurring downstream in the visual pathway, does not require optical transparency and could be effective in cases of eye trauma. Here we show, in anaesthetized rabbits and with support from numerical modelling, that an intraneural electrode array with high mechanical stability placed in the intracranial segment of the optic nerve induces, on electrical stimulation, selective activation patterns in the visual cortex. These patterns are measured as electrically evoked cortical potentials via an ECoG array placed in the contralateral cortex. The intraneural electrode array should enable further investigations of the effects of electrical stimulation in the visual system and could be further developed as a visual prosthesis for blind patients.

Visual prostheses have recently emerged as tools to fight blindness, a medical condition affecting more than 30 million people worldwide¹. Starting from early pioneering works^{2,3}, over the past 50 years, several types of visual prostheses have been proposed and classified by their location along the visual pathway^{4,5}, including subretinal⁶, epiretinal⁷, suprachoroidal⁸, optic-nerve⁹, thalamic¹⁰ and cortical prostheses¹¹. Retinal implants quickly became the preferred strategies, since they can benefit from natural information processing along the visual pathway¹². In various clinical trials, retinal prostheses have demonstrated the capability to restore a functional form of vision^{13,14}. Today, several research groups are developing retinal prostheses, with a special emphasis on light-driven photovoltaic implants^{15–19}. However, optic-nerve stimulation is also an attractive strategy, since it bypasses the entire retinal network and directly activates nerve fibres. Further, like epiretinal prostheses, it still takes advantage of the high-level information processing occurring downstream in the visual pathway. Moreover, optic-nerve stimulation could be effective in cases of severe trauma (such as retinal detachment or eyeball trauma) and does not require optical transparency (for example, in the case of corneal opacities). Indeed, history of retinal detachment, trauma and severe strabismus are among the contraindications for the Argus II epiretinal prosthesis.

Optic-nerve stimulation was pioneered with the implantation in the intracranial segment of a blind subject of a four-contact self-sizing spiral cuff epineural electrode array²⁰, in which electrical stimuli elicited localized phosphenes. After a few months of training and psychophysical testing, the patient was able to distinguish line orientations as well as shapes and symbols despite using only four electrodes. Another patient was later implanted with an eight-contact electrode²¹, confirming the possibility of restoring functional vision via optic-nerve stimulation^{22–24}. However, in

these trials, the induced phosphenes were reported as irregular; the use of spiral cuff epineural arrays could be the cause²⁵ because of their limited mechanical stability. Following these results, the C-Sight project is currently investigating an optic-nerve prosthesis based on an array of three penetrating metal electrodes to stimulate the intraorbital segment of the optic nerve in rabbits^{26,27} and cats²⁸. This project employs penetrating platinum–iridium electrodes, which are characterized by high stiffness (Young's modulus of approximately 100 GPa) and rigidity, inducing a large mechanical mismatch with the nerve, which could have negative consequences for chronic implantation. Conversely, transverse intrafascicular multichannel electrode (TIME) arrays, microfabricated using thin-film technology, have already demonstrated their superior capability in peripheral nerve stimulation^{29,30}. TIME arrays showed better mechanical compliance (Young's modulus of approximately 1 GPa and high flexibility) compared with penetrating metal electrodes, and higher selectivity in fibre stimulation compared with spiral cuff epineural arrays^{31,32}. More recently, a self-opening intraneural electrode (SELINE) array demonstrated improved mechanical stability compared with TIME arrays³³ as well as high biocompatibility over a period of six months³⁴. In this work, we exploited OpticSELINE, a modified version of the previously described SELINE array^{33,34}, as a visual prosthesis based on optic-nerve stimulation.

Results

Electrode array design and characterization. The OpticSELINE is a polyimide-based looped electrode array designed in agreement with the anatomical structure of the rabbit's optic nerve, which has a mean (\pm s.d.) diameter of 1.45 ± 0.10 mm (Supplementary Fig. 1). Each side has a total length of 33 mm, a maximum width of 3 mm and an overall thickness of 12 μ m (Fig. 1a). A 35 mm polyimide-based extension flat cable enables connection between the electrode array

¹Medtronic Chair in Neuroengineering, Center for Neuroprosthetics and Institute of Bioengineering, School of Engineering, École polytechnique fédérale de Lausanne, Geneva, Switzerland. ²The BioRobotics Institute, Scuola Superiore Sant'Anna, Pisa, Italy. ³Bertarelli Foundation Chair in Translational Neuroengineering, Center for Neuroprosthetics and Institute of Bioengineering, School of Engineering, École polytechnique fédérale de Lausanne, Geneva, Switzerland. ⁴These authors contributed equally: Vivien Gaillet, Annarita Cutrone, Fiorenzo Artoni. ⁵These authors jointly supervised this work: Silvestro Micera, Diego Ghezzi. *e-mail: diego.ghezzi@epfl.ch

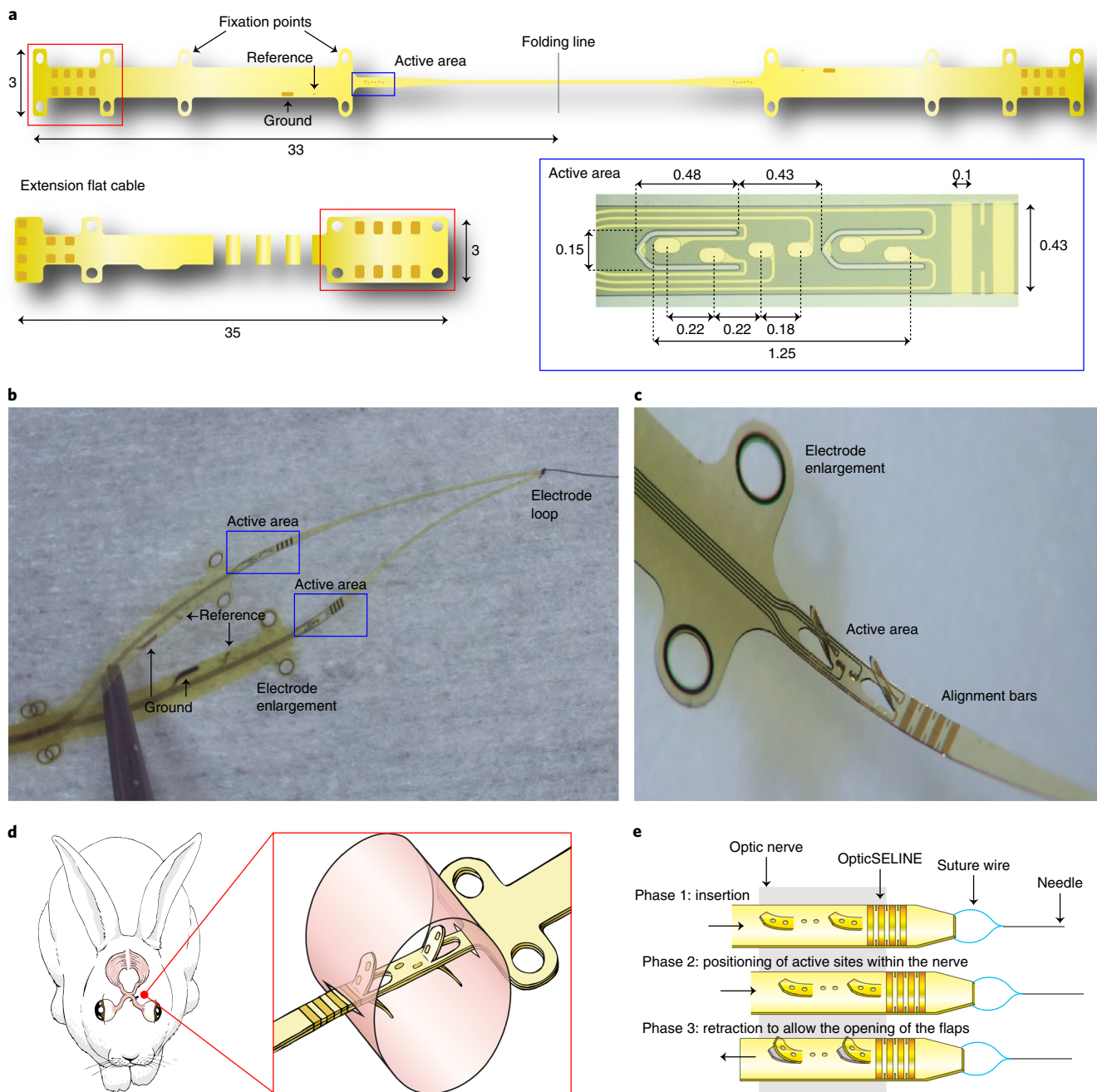


Fig. 1 | The intraneural electrode array OpticSELINE. **a**, Sketch of the OpticSELINE. The red box highlights the connection area between the electrode and the flat cable terminated with an Omnetics connector mounted on a printed circuit board (not shown). The blue box highlights one active area where two flaps and six electrodes are visible. Dimensions are in mm. **b**, Photograph of the OpticSELINE, showing the looped structure with two active areas. **c**, Magnified view of one side of the OpticSELINE, showing the active area with the flaps after three-dimensional shaping, the electrodes and the alignment bars. The electrode enlargement is used as a stopper to avoid excessive insertion of the array within the nerve. **d**, Sketch of the OpticSELINE implanted in the rabbit optic nerve. The red box shows details of the implanted OpticSELINE in the optic nerve (cylindrical shape). **e**, Schematic of the insertion procedure.

and the head-fixed plug connector. Each side of the OpticSELINE has six stimulating electrodes (each with an area of 0.008 mm^2) and a reference and a ground electrode outside the active area (Fig. 1b). Two three-dimensional flaps extend from both sides of the main body and carry two electrodes each; two more electrodes are located on each side of the main body. Each flap has a width of 0.15 mm and a length of 0.48 mm . The width of the active area is 0.43 mm and the length is 1.25 mm . Four alignment bars (width of 0.1 mm) were included to ease the insertion procedure and verify that the

active area is located inside the optic nerve (Fig. 1c). The insertion procedure follows a standardized technique that was previously validated in the peripheral nerves of both animals³⁴ and humans^{29,30}. A suture with a needle guides the OpticSELINE transversally into the nerve until the electrode enlargement is reached (used as a stopper); at this stage, the four alignment bars are visible outside of the nerve. The OpticSELINE is then slightly pulled back until only three alignment bars are visible to anchor the flaps into the nerve (Fig. 1d,e).

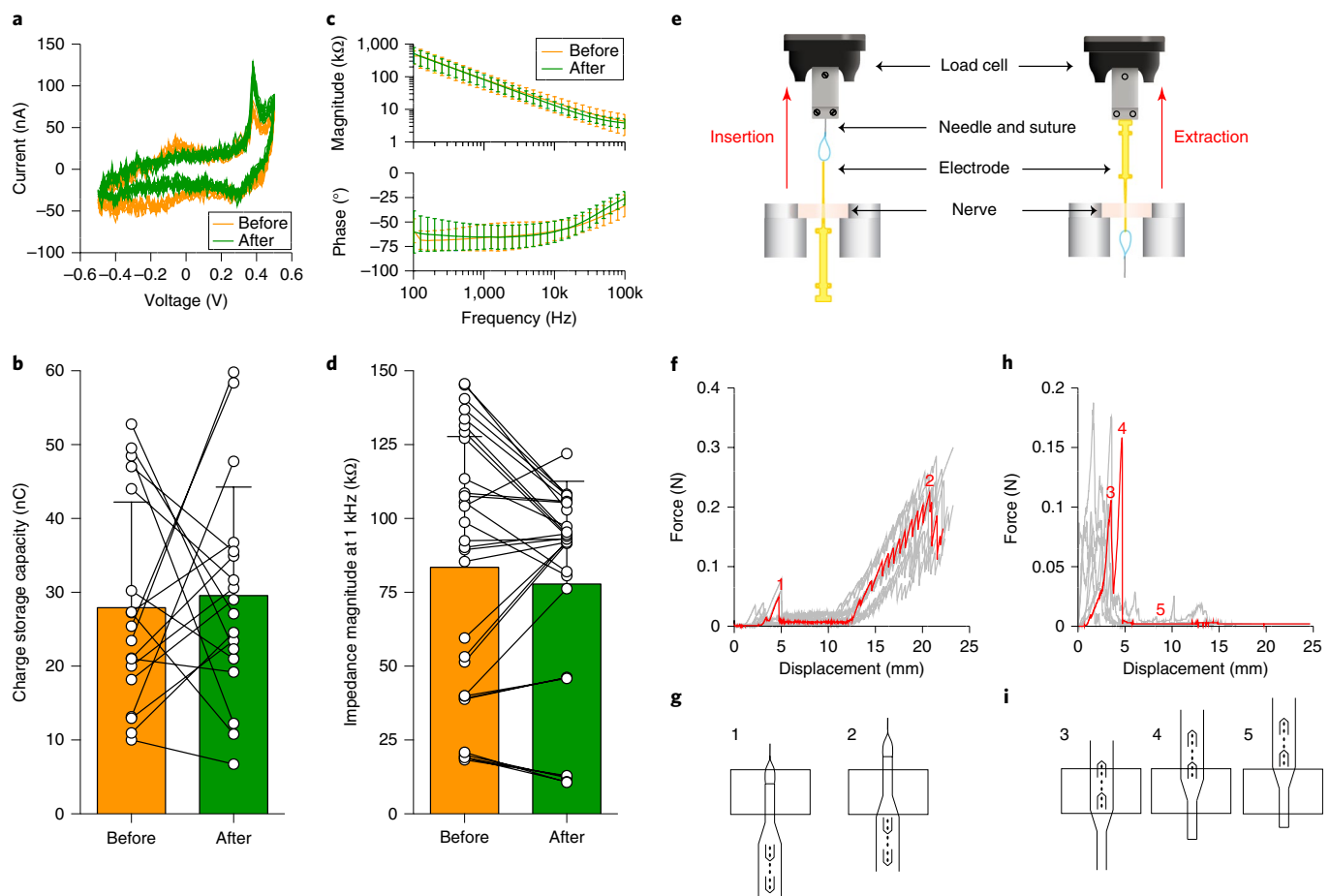


Fig. 2 | Electrochemical and mechanical characterization. **a**, Cyclic voltammetry performed on the electrodes before (orange) and after (green) passive accelerated ageing. Representative example of 1 electrode with an overlay of 10 repetitions. Experiment repeated on $n=18$ electrodes from 4 OpticSELINEs. **b**, Quantification of the mean (\pm s.d.) charge storage capacity ($n=18$ electrodes from 4 OpticSELINEs). **c**, Mean (\pm s.d.) magnitude (top) and phase (bottom) of the electrode impedances before (orange) and after (green) passive accelerated ageing ($n=30$ electrodes from 4 OpticSELINEs). **d**, Quantification of the mean (\pm s.d., $n=30$ electrodes from 4 OpticSELINEs) impedance magnitude at 1 kHz. **e**, Schematic of the ex vivo insertion (left) and extraction (right) experiments in explanted optic nerves from New Zealand white rabbits. **f**, Forces during insertion in the optic nerve. Several insertion trials ($n=10$ trials) are shown in grey. A selected example (red) is labelled with the different phases of insertion. **g**, Sketch showing the different phases of insertion (phase 1 and phase 2). **h**, Forces during extraction from the optic nerve. Several extraction trials ($n=10$ trials) are shown in grey. A selected example (red) is labelled with the different phases of extraction. **i**, Sketch showing the different phases of extraction (phases 3, 4 and 5).

First, we characterized both the electrochemical and mechanical properties of the OpticSELINE. Cyclic voltammetry was performed to determine the charge storage capacity of the electrodes (Fig. 2a) before and after a passive accelerated-ageing equivalent to an implantation time of 6.4 months (6 d at 87°C)³⁵. The mean (\pm s.d.) charge measured before (27.95 ± 14.28 nC) and after (29.55 ± 14.70 nC) ageing were not significantly different (Fig. 2b; $n=18$ electrodes from 4 OpticSELINEs; $P=0.75$, two-tailed paired t -test). Given the small electrode area (0.008 mm^2), these values of charge storage capacity (0.35 and 0.37 mC cm^{-2} , respectively, before and after ageing) are comparable to the values found in the literature for gold microelectrodes³⁶. Similarly, we performed impedance spectroscopy (Fig. 2c); the mean (\pm s.d.) magnitude at 1 kHz was not significantly different before ($83.52 \pm 44.27\text{ k}\Omega$) or after ($77.79 \pm 34.86\text{ k}\Omega$) ageing (Fig. 2d; $n=30$ from 4 OpticSELINEs; $P=0.18$, two-tailed paired Wilcoxon test).

A mechanical characterization was performed to verify the compatibility of the electrode array with the insertion forces and the stability within the optic nerve of New Zealand white rabbits. During insertion experiments (Fig. 2e, left), two major force peaks were observed (Fig. 2f,g), corresponding to the insertion of the loop

inside the nerve (peak 1) and to the entry of the enlarged area of the device (peak 2). The mean (\pm s.d., $n=10$ trials) insertion forces are $32.5 \pm 22.7\text{ mN}$ (peak 1) and $223.4 \pm 92.2\text{ mN}$ (peak 2). The stability of the electrode within the nerve was evaluated with an extraction experiment (Fig. 2e, right). During extraction, two major force peaks were observed (Fig. 2h,i), corresponding to the force necessary to extract the three-dimensional flaps (peaks 3 and 4), followed by a flat phase relative to the slippage of the loop through the nerve (5). The mean (\pm s.d., $n=10$ trials) extraction forces are $101.2 \pm 36.2\text{ mN}$ (peak 3) and $100.3 \pm 38.5\text{ mN}$ (peak 4), 30 times larger than the mean (\pm s.d.) force required to extract a similar electrode array without three-dimensional flaps ($3.2 \pm 0.5\text{ mN}$; $n=4$ trials). This latter value is similar to what was previously measured in the rat sciatic nerve³³. This confirms that the three-dimensional flaps enhance the anchorage of the OpticSELINE within the nerve and provide better mechanical stability compared to TIME electrodes.

Visual stimulation. In the first set of rabbits, we characterized visually evoked cortical potentials (VEPs) on flash stimulation (4 ms, Ganzfeld white LED; Fig. 3a). The peak amplitudes (PAs) and latencies (PLs) of the two major peaks present in the VEP

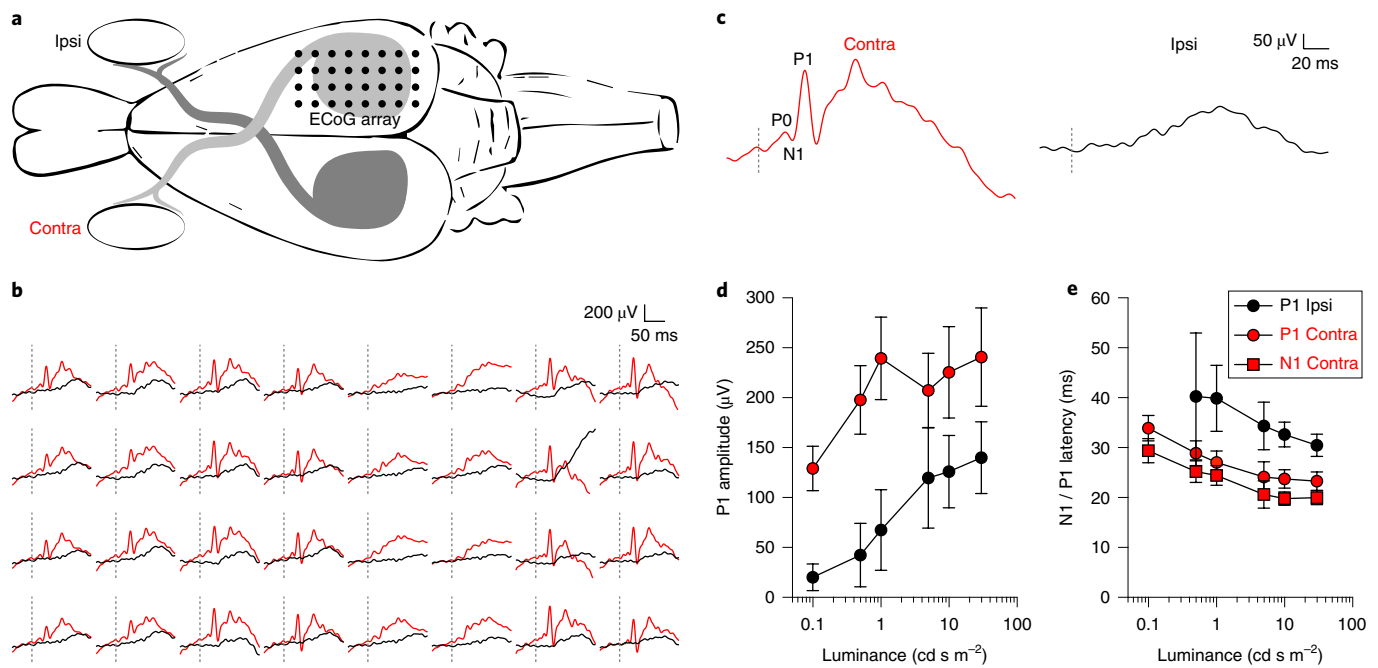


Fig. 3 | Visually evoked cortical potentials. **a**, Schematic diagram (top view) of the placement of the ECoG array (black dots) over the rabbit visual cortex. Recordings of VEPs were performed with the ECoG array upon flash stimulation (4 ms, Ganzfeld white LED) of both the ipsilateral (black) and contralateral (red) eye. **b**, Example of traces (synchronous average of 10 responses) to a flash illumination of 0.5 cd s m^{-2} at the ipsilateral (black) or contralateral (red) eye. The dashed lines represent the occurrence of the flash. Experiment repeated on $N=9$ rabbits. **c**, Example traces obtained from the average of the 32 recording channels (shown in **b**) for both ipsilateral (black) and contralateral (red) stimulation. P0, N1 and P1 peaks are visible (N for negative potential and P for positive potential). The dashed lines represent the occurrence of the flash. Experiment repeated on $N=9$ rabbits. **d,e**, Quantification of the P1 PA (**d**) and PL (**e**) as a function of the flash luminance. Each data point is the mean (\pm s.e.m.) of $N=9$ rabbits. For each rabbit, ten consecutive recordings were averaged. For each recording, the 32 recording channels were averaged.

(N1 and P1) were measured using an electrocorticography (ECoG) electrode array (Fig. 3b). The ECoG consists of a 4×8 array with $200 \mu\text{m}$ platinum electrodes with a 1 mm pitch (E32-1000-30-200; NeuroNexus). The ECoG was placed over V1 visual cortex; given its small size, it is unlikely that it covers other areas than V1. However, we cannot formally exclude this possibility. We stimulated each rabbit on both eyes (ipsilateral and contralateral relative to the ECoG array) with flashes of increasing luminance levels ($0.1, 0.5, 1, 5, 10$ and 30 cd s m^{-2}). As expected, the strongest and fastest response occurred for contralateral stimulation (Fig. 3c), since in albino rabbits, 90 to 95% of the optic-nerve fibres decussate at the level of the chiasm³⁷. The cortical activation for ipsilateral stimulation appeared only for luminance levels higher than 1 cd s m^{-2} , at which value the response to the contralateral stimulation was already saturated (Fig. 3d). As previously reported³⁸, the mean (\pm s.e.m., $N=9$ rabbits) P1 PL in contralateral stimulation started at $33.93 \pm 2.59 \text{ ms}$ for low luminance levels (0.1 cd s m^{-2}) and reached a plateau latency of $23.28 \pm 1.86 \text{ ms}$ for luminance levels higher than 5 cd s m^{-2} (Fig. 3e). The mean (\pm s.e.m.) N1 PLs in contralateral stimulation were also comparable with previously reported data³⁸ (Fig. 3e).

Electrical stimulation. In a second set of rabbits, we implanted the OpticSELINE transversally into the optic nerve from the lateral to the medial side. Because of the high percentage of fibre decussation at the level of the chiasm³⁷, electrically evoked cortical potentials (ECPs) were measured by an ECoG array in the contralateral visual cortex (Fig. 4a,b). Cathodic first asymmetrically balanced (1:5) electrical stimuli were used. A previous report demonstrated that the ratio 1:5 is a good compromise between total pulse duration and stimulation efficiency²⁷. The same study also showed that placing the balancing anodic phase before the cathodic stimulation

phase with a 1:5 ratio has no influence on the stimulation efficiency. Moreover, we did not introduce any interphase gap, since it has been demonstrated to have a significant effect only with symmetrically balanced stimuli²⁷. Electrical stimulation consisted of a single biphasic pulse, unless stated otherwise. Upon electrical stimulation of the optic nerve, we found that both N1 and P1 PAs increased with the current amplitude of the stimulus (Fig. 4c). To limit the overall experimental time for each rabbit and to avoid nerve fatigue due to repetitive stimulations (Supplementary Fig. 2a), we used only six electrodes of the OpticSELINE, located on the top side (from 1 to 6), unless stated otherwise.

First, we identified the N1 current threshold (that is, the minimum current required to induce the N1 peak in the EEP) using an automated peak detection algorithm followed by visual inspection and validation. To quantify the N1 current threshold, for each stimulating electrode of the OpticSELINE, we selected among the 32 recording electrodes the one with the highest N1 PA within the series (called the N1 leading channel). In the first rabbit (Fig. 4d), we determined the N1 current threshold as a function of the pulse duration (50, 100, 150, 200 and $400 \mu\text{s}$, cathodic phase). The N1 current threshold decreased with increasing pulse duration. However, for pulses shorter than $100 \mu\text{s}$, there was a minimal effect on the charge (product of the current amplitude per the phase duration) required to induce N1 (Fig. 4e). Then, the charge dropped by increasing the pulse duration from 100 to $150 \mu\text{s}$ and remained stable for longer pulses (Fig. 4e). For pulse durations of $150 \mu\text{s}$, the mean (\pm s.d., $n=6$ electrodes in $N=1$ rabbit) current threshold was $76.77 \pm 66.38 \mu\text{A}$, and the charge threshold was $11.50 \pm 10.02 \text{ nC}$. The electrodes located on the main body (electrodes 3 and 4) showed a N1 current threshold higher than the other electrodes (1, 2, 5 and 6) located on the flaps, in particular for short pulses (Fig. 4d).

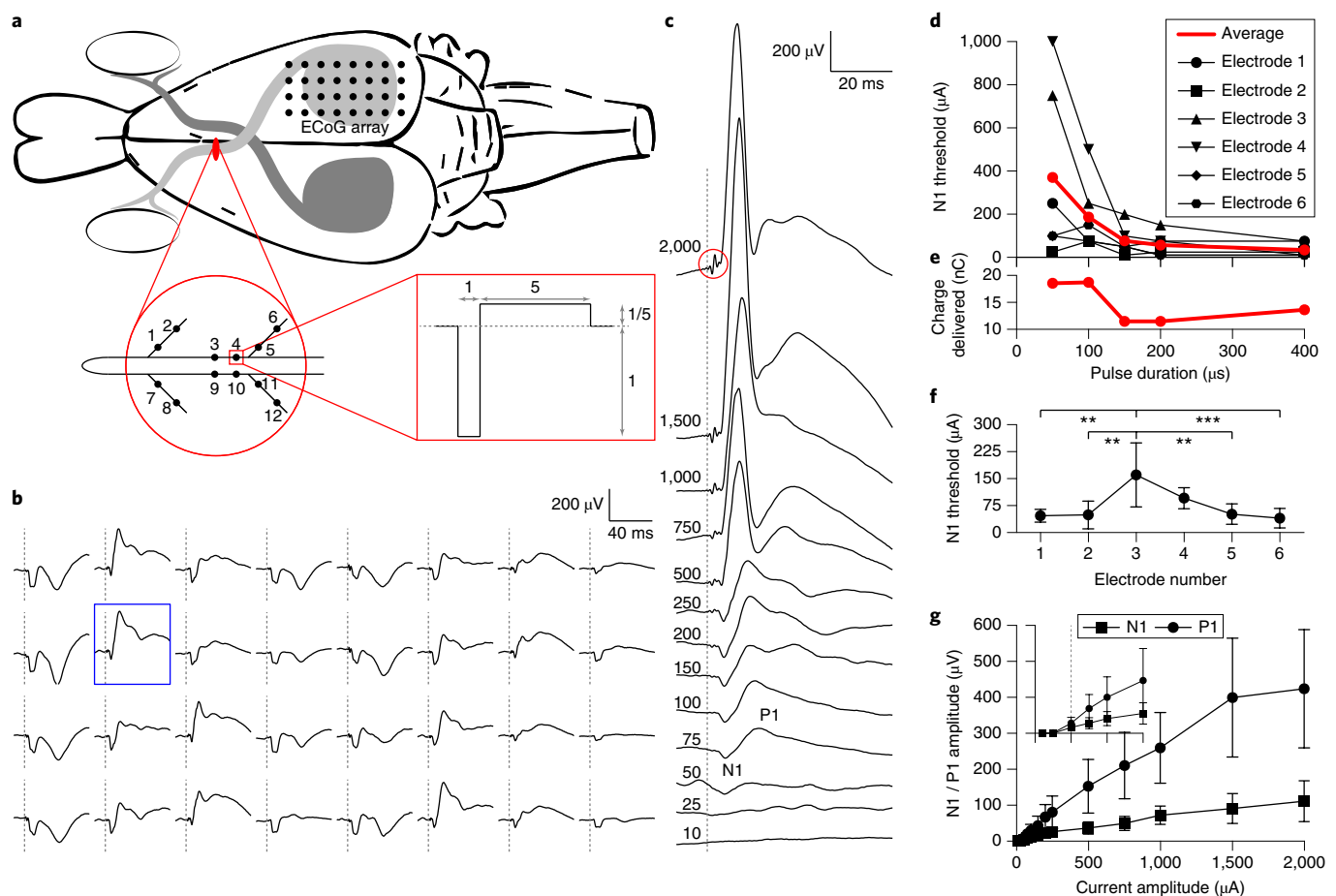


Fig. 4 | Electrically evoked cortical potentials. **a**, Schematic diagram (top view) of the placement of the OpticSELINE in the rabbit optic nerve and of the ECoG array (black dots) over the rabbit visual cortex. The enlarged red circle shows the nerve cross-section with the implanted OpticSELINE. The electrodes are each labelled with a number. EEPs were evoked via the implanted OpticSELINE with biphasic current pulses. The enlarged red box shows the biphasic current pulse delivered from electrode 4. **b,c**, Example of traces (synchronous average of 10 responses) to a current pulse of 250 μA and 150 μs delivered from electrode 4. The dashed lines represent the occurrence of the current pulse. The blue box highlights 1 recording electrode, the responses of which (synchronous average of ten responses) to increasing current pulses (left numbers in μA) of 150 μs are visible in panel **c**. The appearance of N1 and P1 peaks is visible. The dashed line shows the occurrence of the current pulse. The red circle shows the stimulation artefact. Experiment repeated on $N=4$ rabbits. **d**, N1 activation thresholds in $N=1$ rabbit as a function of the pulse duration. The red line and circles are the average of the $n=6$ electrodes of the OpticSELINE (from 1 to 6, top side). **e**, The average activation threshold is converted into the charge delivered. **f**, Mean (\pm s.e.m., $N=4$ rabbits) activation thresholds as a function of the OpticSELINE electrode (from 1 to 6, top side; $p < 0.001$, $F = 6.55$, one-way ANOVA, Tukey's multiple comparisons test). **g**, Mean (\pm s.e.m., $N=4$ rabbits) PAs of N1 (squares) and P1 (circles) for current pulses of 150 μs as a function of the current amplitude. The inset shows a magnification from 0 to 150 μA (x axis) and from 0 to 90 μV (y axis); the dashed line is 50 μA . For each rabbit, ten consecutive recordings were averaged. PAs were quantified for each stimulating electrode of OpticSELINE from the averaged response of the 32 recording electrodes. The resulting values were averaged between stimulating electrodes.

On the basis of the previous results, in all subsequent experiments ($N=4$ rabbits), we fixed the first cathodic phase duration to 150 μs . Under this condition, we determined a mean (\pm s.e.m., $N=4$ rabbits) N1 threshold of $74.03 \pm 13.33 \mu\text{A}$, which corresponded to $11.10 \pm 2.00 \text{ nC}$. These values were very similar to those obtained in the first rabbit at 150 μs . We also found a similar and statistically significant trend ($P < 0.001$, $F = 6.55$, one-way ANOVA, Tukey's multiple comparisons test; $N=4$ rabbits), with the electrodes on the main body showing a higher N1 current threshold (Fig. 4f). This could be explained by the fact that in the pre-chiasmatic segment of the optic nerve, the large diameter fibres are localized more in the periphery of the nerve (Supplementary Fig. 3). Indeed, from the histological examination of an optic-nerve sample, we found that the fibre diameters within the whole nerve followed a unimodal distribution with a median of $0.79 \mu\text{m}$ and a mode of $0.47 \mu\text{m}$. In the central area (green square in Supplementary Fig. 3a), the median of the distribution

was lower than in the periphery (0.75 and $0.82 \mu\text{m}$, respectively; $P < 0.0001$, unpaired t -test). The mean (\pm s.d.) fibre density was not different between the centre and periphery (0.19 ± 0.02 versus 0.19 ± 0.04 , fibres μm^{-2} ; $P = 0.40$, unpaired t -test). The overall mean (\pm s.d.) fibre density was 0.19 ± 0.03 fibres μm^{-2} . However, there may be alternative explanations related to the insertion procedure, which could affect more electrodes on the main shaft by increasing their N1 current threshold.

Next, we applied a detection algorithm to determine the N1 and P1 PAs and PLs. The mean (\pm s.e.m., $N=4$ rabbits) N1 and P1 PAs showed monotonic growth as a function of the current amplitude, and the P1 PA saturated above 1,500 μA (Fig. 4g). From the average PAs, it was also apparent that both N1 and P1 became higher than zero, starting from a current pulse of 50 μA (Fig. 4g, dashed line in the inset). Concerning the PLs, N1 PL was stable over the current range of stimulation used (approximately 3.5 ms), whereas P1 PL

slightly decreased from 7.45 to 5.68 ms with the increase in the current amplitude (Supplementary Fig. 4). Qualitatively, PLs in EEPs were shorter than in VEPs by approximately 15 ms, as previously reported²⁷. This was expected, since electrical stimulation bypasses the transduction step performed by photoreceptors. As a control, in one rabbit, we also verified that, similar to visual stimulation, electrical stimulation induced a small activation of the ipsilateral visual cortex only for high current amplitudes (Supplementary Fig. 5).

Cortical activation map. We then investigated the spatial characteristics of cortical activation upon intraneural stimulation of the optic nerve. A blind-source separation approach based on independent component analysis (ICA)^{39–42} was used to quantitatively extract differences between the EEPs resulting from the stimulation through different electrodes of the OpticSELINE. We hypothesized that each EEP is composed of ‘shared’ and ‘meaningful’ components: the shared components characterized by similar time courses regardless of the stimulating electrode activated in the OpticSELINE, and the meaningful components having time courses specific to a single stimulating electrode (or to a small subset at most). For each rabbit, the ICA was performed on the 32 ECoG recordings to highlight the presence of meaningful components that may be hidden by the shared cortical signal. ICA linearly projects the 32 original time courses onto 32 new maximally independent time courses, called independent components (ICs), as weighted sums of the original time courses. We classified the ICs into different categories on the basis of their time course (Supplementary Fig. 6): artefact (that is, containing the stimulation artefact), noise (that is, containing a high-frequency signal), flat (that is, not containing any peak), common (that is, having a similar time course regardless of the stimulating electrode) and meaningful (that is, having different time courses as a function of the stimulating electrode). Artefact, noise, flat and common ICs were considered shared components. The region of the visual cortex in which each IC is present was determined by plotting the activation map of each IC on the 32 electrodes of the recording array (Fig. 5a).

In a representative example ($N=1$ rabbit, current amplitude of 750 μA), all 12 stimulating electrodes of OpticSELINE were used, and among the 32 ICs, 24 were labelled as meaningful, 4 as common, 1 as flat, 1 as noise and 2 as artefact (Fig. 5b and Supplementary Fig. 7). However, 9 stimulating electrodes (electrodes: 1, 2, 3, 4, 5, 6, 8, 9 and 12) out of 12 resulted in meaningful cortical activation, whereas 3 (electrodes: 7, 10 and 11) induced only flat responses (Supplementary Fig. 8, black traces). By back-projecting only the meaningful ICs onto the original channel space, the original data could also be filtered to highlight only the meaningful components (Supplementary Fig. 8, red traces). By increasing the current amplitude of the pulse, the number of ICs classified as meaningful increased, reaching its maximum value between 500 μA and 1,000 μA and then decreasing (Fig. 5d). This was probably due to the beginning of the saturation of the cortical response; therefore, more ICs are classified as common instead of meaningful. The activation maps of the 24 meaningful ICs show that they are present in distinct regions of the visual cortex (Fig. 5e).

In addition, each meaningful IC exhibited a different degree of activation as a function of the stimulating electrode used. To quantify this, for each meaningful IC, the peak-to-peak amplitude of the early portion of the time courses (from 5 to 25 ms after the pulse) induced by each stimulating electrode was computed and normalized among all the stimulating electrodes. All nine functional stimulating electrodes had at least one meaningful IC whose activation was maximized when stimulating through this electrode. Furthermore, by interpolating the contribution of every stimulating electrode to each IC, we found their distribution map within the optic nerve. The area corresponding to 90% of the activation level was confined to a small area around this electrode or, in some cases,

it spread over one or two neighbouring electrodes (white lines in Fig. 6a and red lines in Fig. 6b). As expected, the three electrodes associated only with flat responses had no meaningful ICs associated with them. A further classification of meaningful ICs based on the distribution map within the optic nerve revealed that the 24 meaningful ICs could be grouped into 10 meaningful clusters (Fig. 6c). We verified that the number of meaningful clusters did not significantly change when considering less restrictive activation levels. With both 80% and 70% activation levels, the number of meaningful clusters was 9. In addition, in this representative example, the number of meaningful clusters remained qualitatively constant regardless of the current amplitude (Fig. 5d, red trace and symbols).

We obtained a similar result in all the rabbits ($N=4$) recorded by stimulating with only six electrodes of the OpticSELINE (from 1 to 6, top side). On average, with the increase of the current amplitude, the number of flat ICs decreases, the number of common ICs increased, and the number of meaningful ICs first increased and then stabilized (Supplementary Fig. 9). The mean (\pm s.d.) number of meaningful clusters remained qualitatively constant regardless of the current amplitude. The spatial organization of the ICs in the visual cortex and the back-projection of the ICs in correspondence with the OpticSELINE electrodes are considered as indirect signatures of the stimulation selectivity of the OpticSELINE.

Selectivity of optic-nerve stimulation. Measuring the recruitment and activity of optic-nerve fibres during *in vivo* stimulation is a challenging task. In addition, relying on cortical EEPs to determine the threshold and level of optic-nerve activation is critical, since cortical recordings might be affected by the variability in the impedance of the recording electrodes, both intra- and inter-subject. Therefore, to better evaluate the current threshold and the number of fibres activated by each electric pulse at increasing current amplitudes, we implemented a hybrid numerical model and simulation based on two steps^{43,44}. First, the potential field generated by the electrical stimulation was computed using finite element analysis (FEA). Then, the activation probability of the fibres located around the stimulating electrode was obtained using the NEURON simulation environment. For the anatomical model, we considered the fibre distribution according to our findings (Supplementary Fig. 3), and the nerve diameter was set to 1.5 mm. The hybrid FEA model and NEURON simulation showed that on cathodic stimulation with pulses of 150 μs , the activation of nerve fibres started from current amplitudes as low as 2 μA and increased with increasing current amplitudes (Fig. 7a,b). The number of nerve fibres activated was estimated considering a fibre density of 0.19 fibres μm^{-2} , as previously identified (Fig. 7b). These results show that OpticSELINE can activate both internal and external fibres, in contrast to self-sizing spiral cuff epineural electrodes that preferentially activate the latter⁴³. Finally, we investigated the electrode selectivity by computing the overlap of the activated fibres as a function of the stimulating current from two neighbouring electrodes (Fig. 7c,d). The two activated areas remained separated up to a current amplitude of 10 μA , whereas for higher currents, they started to fuse together, reaching a value of 31.2 % for 50 μA .

There is a narrow range over which currents can be varied (up to approximately 10 μA) without affecting the spatial selectivity in fibre recruitment; overall, this limits the dynamic range of intraneural stimulation. However, by using a self-sizing spiral cuff epineural electrode, it has been shown that high-frequency stimulation can be exploited to reduce the perception threshold instead of pulse modulation (amplitude or duration)⁴³. First, we verified that this mechanism can also be recruited with intraneural stimulation via OpticSELINE. We delivered pulse trains (consisting of one, two, three or four pulses) at the highest repetition rate (1 kHz) allowed by our stimulation protocol (Fig. 8a). In this manner, our results can be generalized to every lower repetition rate;

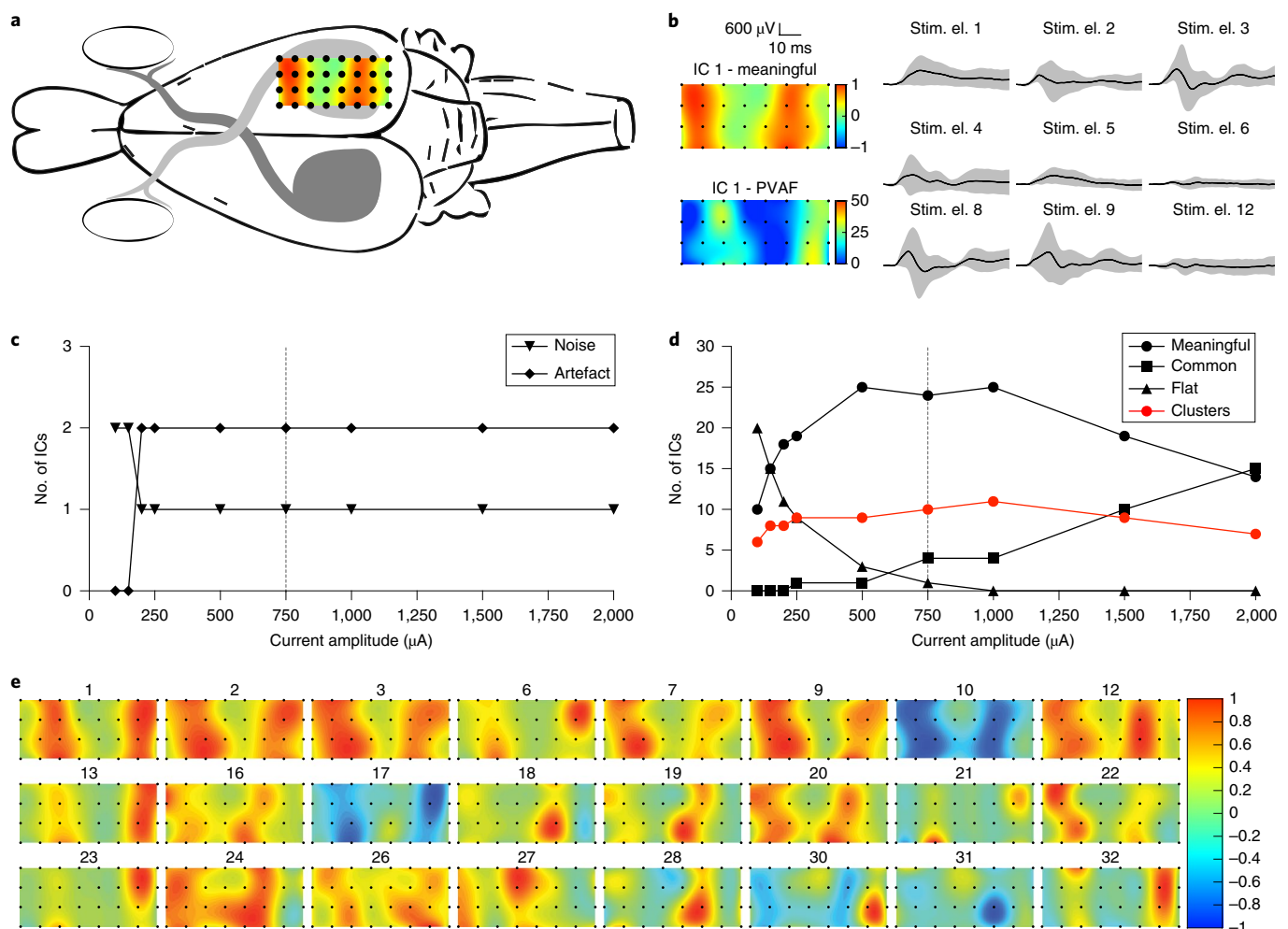


Fig. 5 | Cortical activation maps. **a**, Schematic diagram (top view) of the rabbit visual cortex with an example of an activation map corresponding to IC1 projected onto the ECoG array. **b**, Example of the activation map (the colour code is the weight assigned to the IC), the percentage of variance accounted for (PVAf) and the time courses of a representative meaningful component (IC 1). A time course is shown for each stimulating electrode (stim. el.) of the OpticSELINE. The black lines are the mean of 10 repetitions and the grey shadings are the standard deviation. **c**, Number of ICs classified as artefact or noise as a function of the current amplitude. At low currents (100 and 150 μA), the artefact cannot be detected. Noise ICs decrease from 2 to 1 because IC 4 is first detected as noise IC (100 and 150 μA) and later (>200 μA) detected as artefact IC. The dashed line shows the number of ICs obtained for a current amplitude of 750 μA , the reference value used in **e**. **d**, Number of ICs classified as flat, common and meaningful as a function of the current amplitude. The number of meaningful clusters is plotted in red. The dashed line shows the number of ICs and clusters obtained for a current amplitude of 750 μA , the reference value used in **e**. **e**, The 24 meaningful ICs are present in distinct regions of the visual cortex. The colour code is the weight assigned to the IC. Representative example from $N=1$ rabbit with a current amplitude of 750 μA . Experiment repeated on $N=4$ rabbits.

for example, as previously shown up to 300 Hz⁴³. We also verified that nerve fatigue due to repetitive stimulation with a pulse train is not present (Supplementary Fig. 2b–d). By increasing the number of pulses within the train (from 1 to 4) with equal current amplitude, the mean (\pm s.e.m., $N=4$ rabbits) N1 threshold was reduced to $35.83 \pm 6.59\%$ (for four pulses) of the threshold obtained with a single pulse (Fig. 8b). Similarly, cortical activation (for example, P1 PA) can be modulated in amplitude by increasing the number of pulses instead of changing the current intensity (Fig. 8c). Notably, by using the hybrid FEA model and NEURON simulation, we estimated that the activated area from each electrode was not affected (maximal variation of 4.3% for a current pulse of 15 μA) by increasing the number of pulses in the train while keeping the amplitude constant (Fig. 8e); this is particularly evident for current amplitudes below 10 μA . In a previous study, this phenomenon was reported as a mechanism of temporal summation (Fig. 8d) resulting from the repeated activation of the same few axons and

not leading to the recruitment of more fibres. This strategy based on frequency modulation can be applied to widen the input dynamic range of the OpticSELINE. In addition, techniques such as current steering and focusing might be used to further enhance the stimulation selectivity⁴⁴.

Discussion

Currently, research on visual prostheses is mostly focused on the development of retinal prostheses, either subretinal, epiretinal or suprachoroidal^{15,16,18,19,45–48}. Nevertheless, in addition to the early pioneering works, some research groups are attempting the stimulation of other regions of the visual pathway¹². Optic-nerve prostheses aim to stimulate the axonal fibres from retinal ganglion cells along their path towards the optic chiasm. Optic-nerve stimulation was first reported in a set of studies on two blind patients affected by retinitis pigmentosa^{20,21} and then in another study targeting the optic disc⁴⁹.

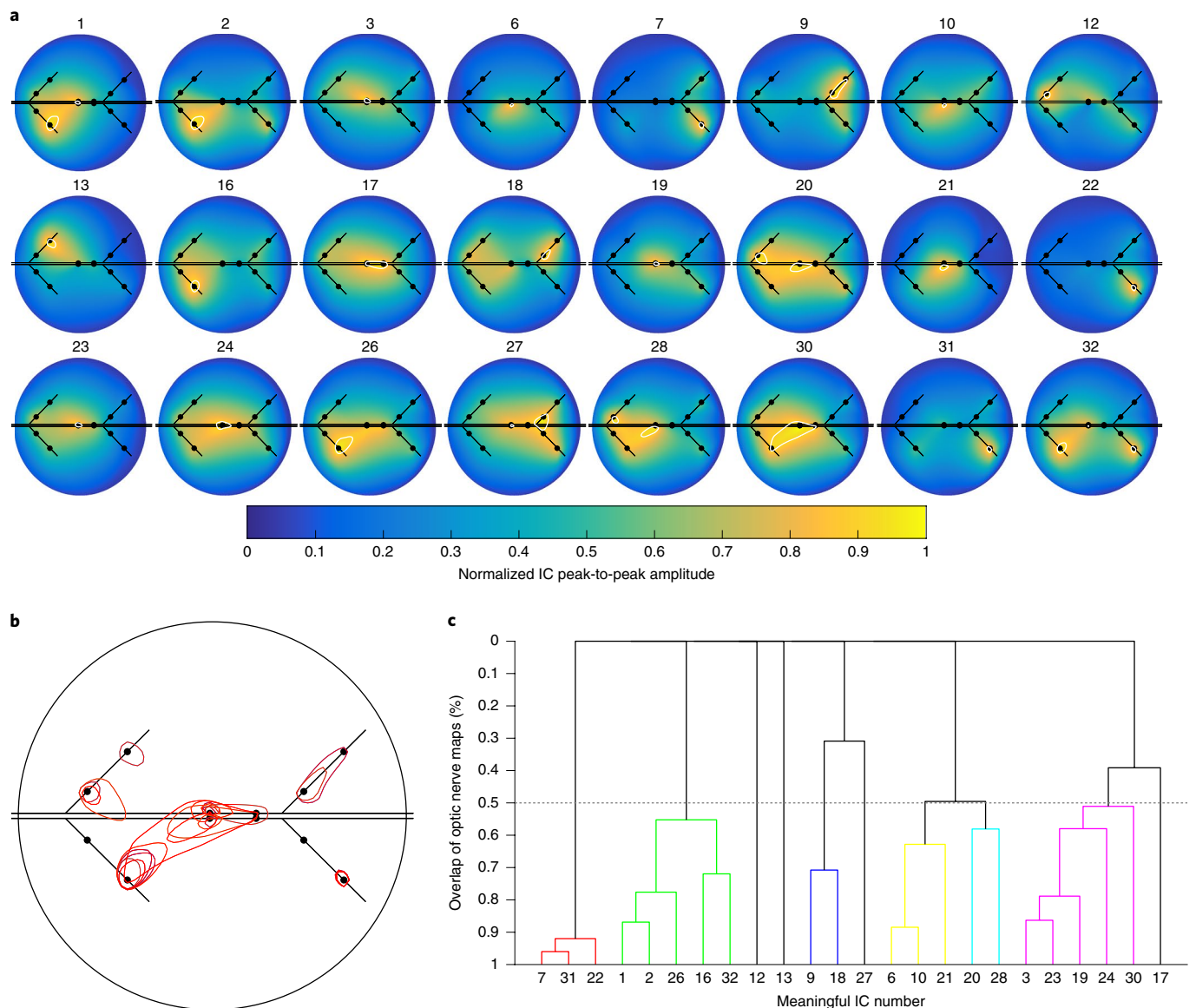


Fig. 6 | Distribution map of the independent components within the optic nerve. a, Individual distribution maps of each meaningful IC within the optic nerve. The colour code is the normalized IC peak-to-peak amplitude. The white contour corresponds to 90% of the maximal value of the distribution map. Most of the meaningful ICs are segregated in a small portion of the optic nerve, localized around one or in some cases a few neighbouring electrodes. **b**, Overlay of the 90% activation contours (red) of all the meaningful ICs. The black circle represents the optic nerve. The sketch of the OpticSELINE is in black in both **a** and **b**. **c**, Dendrogram of the hierarchical clustering of the meaningful ICs, based on the average overlap between the 90% area of each of their distribution maps at the level of the optic nerve. The threshold to determine the meaningful ICs that are part of the same cluster was set to a minimum overlap of 50% (dashed line). Representative example from $N=1$ rabbit with a current amplitude of $750\mu\text{A}$. Experiment repeated on $N=4$ rabbits.

In the first set of studies, the two patients were implanted with self-sizing spiral cuff epineural electrodes, which have the advantage of being less invasive than intraneural arrays. However, one of the main limitations of the self-sizing spiral cuff epineural electrode is the induction of phosphenes that are widely distributed in the visual field of the patient, probably because they mostly activate external fibres with limited selectivity⁴³. Nevertheless, intraneural arrays can also stimulate the central area of the nerve and provide higher stimulation selectivity³². In addition, intraneural arrays such as the OpticSELINE are mechanically very stable³³; therefore, they could enable more reproducible and stable stimulation. For these reasons, we selected an intraneural approach, confirming the high mechanical stability provided by the lateral flaps and the high selectivity in fibre recruitment, as demonstrated by the hybrid FEA model and NEURON simulation.

In our experimental design, we chose to target the intracranial segment of the optic nerve. Spiral cuff epineural electrodes were previously implanted in both the intraorbital²¹ and intracranial²⁰ segment of the nerve. The comparison of the two clinical studies showed that intraorbital stimulation induces smaller EEPs compared with intracranial stimulation, whereas latencies are not significantly different; in other words, the perceptual threshold is higher for intraorbital stimulation⁹. In addition, the intraorbital segment of the optic nerve must accommodate eye movements; therefore, an intraneural electrode may be subjected to high cyclic strain, which could lead to subsequent failure. This issue is minimized in the intracranial segment. A third drawback of the intraorbital placement of an intraneural electrode is due to the presence of the central retinal vein and artery entering the nerve at approximately 1 cm from the eyeball; an intraneural placement may risk damaging

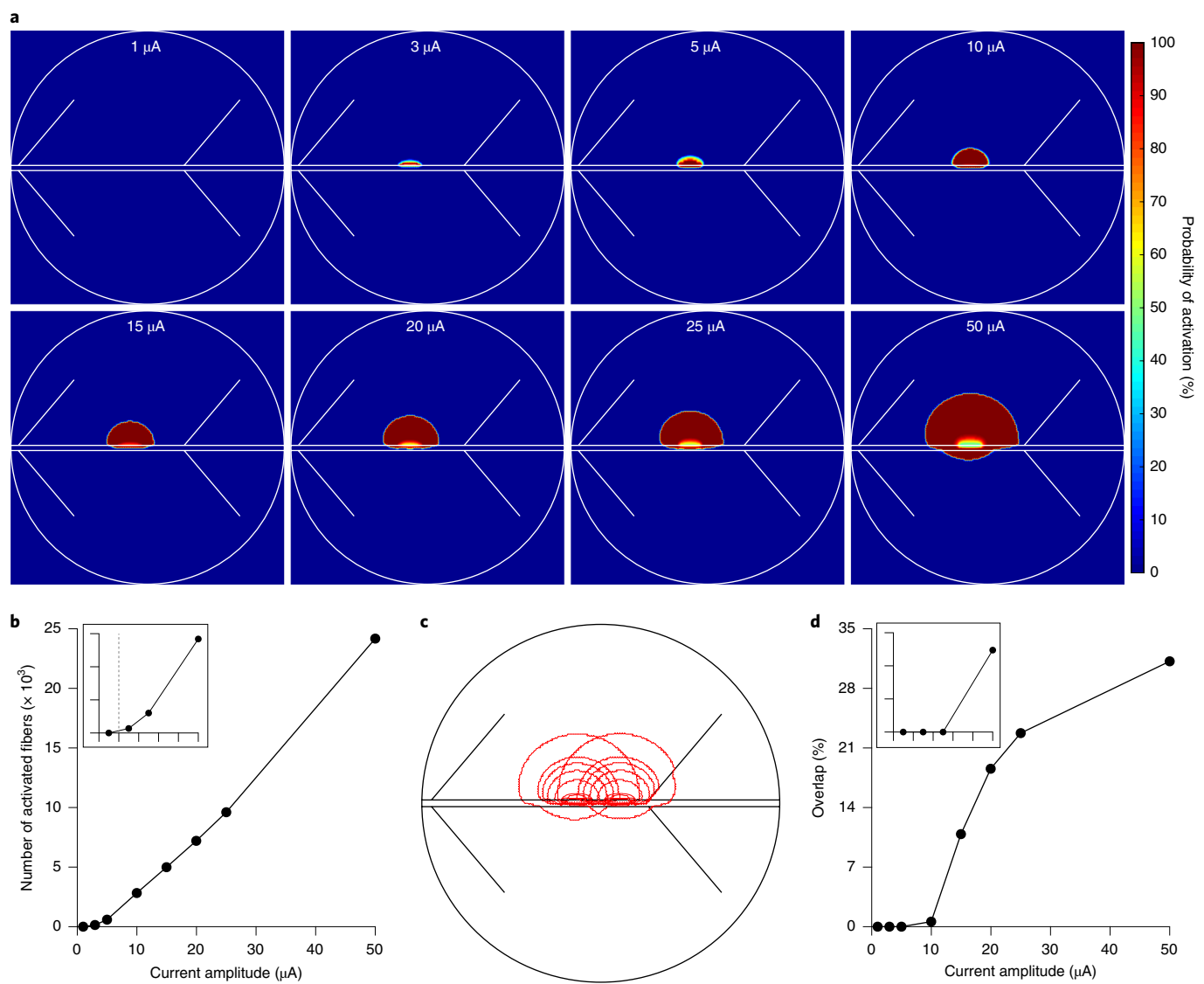


Fig. 7 | Probability activation map of the optic nerve. a, Probability activation map upon current pulses (150 μs , cathodic phase first) at increasing current amplitudes from electrode 3 of the OpticSELINE. The colour code is the probability of activation in percentage. **b**, Number of fibres activated by a single current pulse as a function of the current amplitude. The inset graph shows a magnification from 0 to 10 μA (x axis) and from 0 to 3,000 fibres (y axis); the dashed line is 2 μA . **c**, Overlay of the activated area with a probability higher than 90% at increasing current amplitudes for electrodes 3 and 4. **d**, Per cent overlap of the activated areas from electrodes 3 and 4 as a function of the current amplitude. The inset graph shows a magnification from 0 to 10 μA (x axis) and from 0 to 0.75% (y axis).

them. Therefore, for intraneural electrodes, the intracranial placement seems more appropriate than intraorbital placement.

In a previous study with the self-sizing spiral cuff epineural electrode⁴³, the perception threshold of the patient was investigated as a function of the stimulation intensity (pulse duration or amplitude) and the stimulation frequency (number of pulses and repetition rate). A reduction of the perception threshold was observed by increasing both parameters: a mechanism of spatial summation (each single pulse recruits more fibres) was associated with the intensity modulation, while a mechanism of temporal summation (repeated activation of the same axons not resulting in the recruitment of more fibres) was associated with the frequency modulation. Although the first mechanism was expected, the second one was more difficult to assess. We showed that intraneural optic-nerve stimulation can be implemented even at a very high frequency (that is, 1 kHz), three times higher than has been previously reported⁴³. As expected, a reduction of the N1 activation threshold was observed

with multiple pulses, without inducing nerve fatigue upon repetitive stimulation. In addition, using a hybrid FEA model and NEURON simulation approach, we verified that the temporal summation does not induce the recruitment of more nerve fibres.

Optic-nerve stimulation differs from retinal prostheses since it selectively activates only axonal fibres instead of cell bodies and other synaptically connected cells in the retinal network; thus, the generated signal is not dependent on the complex and uncontrolled synaptic processing within the retina²³. Subretinal prostheses activate retinal ganglion cells preferentially through the inner nuclear layer. Epiretinal prostheses activate retinal ganglion cells both directly and indirectly via the inner nuclear layer. Short electric pulses preferentially activate retinal ganglion cells directly, even if the thresholds for direct and indirect activation are barely discriminable for clinically used pulses (for example, 450 μs in Argus II)^{50,51}. For this reason, optic-nerve stimulation appears to be a good strategy for neuromorphic prostheses or for the testing of neuromorphic

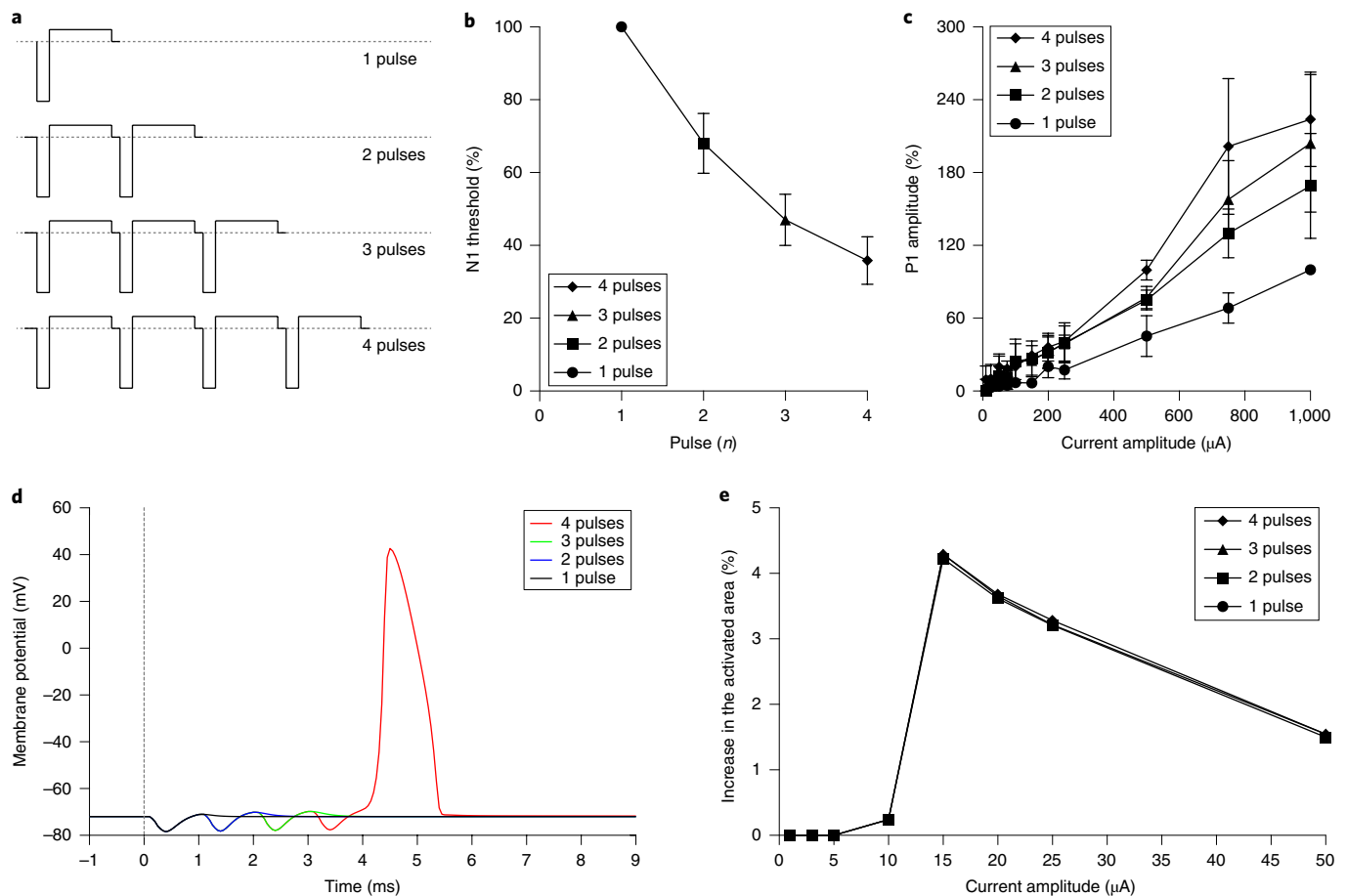


Fig. 8 | High-frequency stimulation of the optic nerve. **a**, EEPs have been evoked via the implanted OpticSELINE (6 electrodes, top side) with biphasic current pulses arranged in packages containing 1, 2, 3 or 4 pulses at 1 kHz of repetition rate. **b**, Normalized mean (\pm s.e.m., $N=4$ rabbits) of the N1 current threshold with stimuli composed of 1 to 4 pulses (circles, squares, triangles and diamonds, respectively). The N1 current threshold was quantified based on the N1 leading channel. For each rabbit, 10 consecutive recordings were averaged. The normalization was performed compared to the threshold on one pulse. **c**, Normalized means (\pm s.e.m., $N=4$) of P1 PAs for trains with 1, 2, 3 or 4 pulses (circles, squares, triangles and diamonds, respectively). The normalization was performed compared to the amplitude on one pulse at 1,000 μ A. For each rabbit, 10 consecutive recordings were averaged. PAs were quantified for each stimulating electrode of the OpticSELINE from the averaged response of the 32 recording electrodes and the resulting values were averaged among stimulating electrodes. **d**, Membrane potential of a simulated optic-nerve fibre upon stimulation with a train composed of 1, 2, 3 or 4 pulses. The current pulse is set to 25 μ A. **e**, Change in the activated area as a function of the current amplitudes for trains with 1, 2, 3 or 4 pulses.

algorithms in animal models, in which the reproduction of the natural code of retinal ganglion cells is needed with high temporal fidelity^{52,53}. Conversely, the downside of optic-nerve stimulation is the inability to activate the inner retinal circuit, which might provide a more natural form of vision.

An important feature of OpticSELINE is the capability to induce selective optic-nerve stimulation and generate spatially organized cortical patterns. The first clinical trial with epineural electrodes already demonstrated that optic-nerve stimulation induces spatially organized phosphenes²³. The C-Sight project demonstrated that in rabbits the position of the cortical channel with the highest amplitude can be spatially modulated by applying current-steering methods to the intraneural stimulation of the intraorbital segment of the optic nerve²⁶. We have found that with an intraneural array, it is possible to associate ‘meaningful’ cortical activation patterns obtained by ICA with specific stimulating electrodes, suggesting that the OpticSELINE induces activation of the visual cortex in a reproducible and spatially organized manner. This is possible because of the selective activation of nerve fibres, which could open the possibility to elicit behaviourally relevant visual activation patterns by optimizing the stimulation protocol.

Outlook. This work contributes to progress towards the implementation of optic-nerve stimulation to restore functional vision. However, our results, obtained in an animal model, cannot be easily translated to restore vision in a blind patient. ECoG recordings measure an integrated activation of the cortical surface, therefore intrinsically lack the required spatial selectivity to prove that different electrodes of the OpticSELINE activate different regions of the visual cortex. To overcome this problem, we implemented a blind source separation approach, which has already been exploited to overcome the intrinsic limitation of the recording method³⁹; for example, to determine different sources of activity in the electroencephalographic signal. Further work is still required to find a direct link between ICs and physiological steady measures such as dipolarity. In addition, further evidence might be obtained with techniques that enable higher specificity in cortical recordings in large animals, such as fast three-dimensional functional imaging tools^{54–56}.

Methods

Electrode microfabrication. OpticSELINE was developed using micro-photolithography and thin-film techniques. A silicon wafer was used as a sacrificial layer. After the cleaning of a silicon wafer (10 min acetone; deionized water rinse;

10 min isopropanol), two layers of polyimide PI2610 (HD MicroSystems) were spun on the substrate (2,000 r.p.m. for 30 s). Samples were hard baked in an oven with nitrogen flux at 350 °C for 1 h. Liftoff layer and S1813 (Microposit) were spin-coated on the wafer at 1,000 r.p.m. for 20 s and 4,500 r.p.m. for 30 s. The substrate was exposed using a glass photomask at a dose of 180 mJ cm⁻². The sample was developed in MF319 for 30 s and rinsed in deionized water. A layer of titanium (20 nm) and gold (250 nm) was sputtered on the substrate and a lift-off technique was used to release the pattern of traces, active sites and pads (overnight immersion in remover 1165). Two layers of PI2610 were spun on the substrate (2,000 r.p.m. for 30 s) and hard baked in the oven with nitrogen flux at 350 °C for 1 h. An aluminium mask (200 nm) was deposited on the substrate by thermal evaporation. S1813 was spun on the sample and exposed (glass photomask, 180 mJ cm⁻²) and the wafer was developed in MF319 for 30 s. S1813 was removed (2 min in remover 1165) and dry etching was used to etch the excess of polyimide (40 sccm of O₂ (sccm, standard cm³ per min); 150 W, 1 h). The aluminium mask was etched away and electrodes were peeled off from the wafer. The three-dimensional geometry was conferred to the OpticSELINE by securing the device on a stainless-steel mould. The mould has four holes in correspondence with the four flaps; a needle was used to secure each flap inside the hole. Alignment holes were included on the mould to ease the placement of the device. A thermal treatment (1 h, 200 °C) was used to memorize the curved shape of the flaps. The devices were connected to the polyimide-based extension cable: a silver conductive glue was used to connect the corresponding pads of the two elements (Ablestik-Henkel; 1 h at 130 °C). Then, the flexible extension cable was connected to a printed circuit board by silver conductive glue. A surgical needle with a looped wire (Ethicon) was inserted through the device. Flexible wires were soldered to the printed circuit board and a linear Omnetics connector was attached. Two-component biocompatible silicone (Silbione-Bluestar Silicones) was applied to all the soldering.

Electrochemical characterization. Cyclic voltammetry was performed using a three-electrode setup immersed in phosphate-buffered saline (PBS) solution and applying a ten-cycle potential ramp at a scan rate of 1.5 V s⁻¹ between -0.5 V and +0.5 V. Impedance measurements were performed using a three-electrode setup immersed in PBS solution and applying a sinusoid of 10 mV between 100 Hz and 100 kHz. The accelerated ageing test was performed for 6 d at a temperature of 87 °C with an accelerating factor of 32. OpticSELINE arrays were in glass beakers filled with PBS and the beakers were sealed and stored in an oven.

Mechanical tests. Both experiments were performed using the same setup, comprising a press to secure the nerve, a 10 N load cell and an explanted rabbit optic nerve. During insertion experiments, the nerve was first pierced by the needle and then the electrode was pulled at a constant speed of 15 mm min⁻¹ to insert the device inside the nerve. During extraction experiments, the device was first implanted inside the nerve, and then the electrode was pulled at a constant speed of 15 mm min⁻¹ to completely extract the device from the nerve. In both cases, insertion and extraction forces were measured by a load cell.

Animal handling and surgery. Animal experiments were performed under the authorization GE1416 approved by the Département de l'Emploi, des Affaires Sociales et de la Santé, Direction Générale de la Santé of the République et Canton de Genève (Switzerland). Female New Zealand white rabbits (>16 weeks, >2.5 kg) were sedated with an intramuscular injection of xylazine (5 mg kg⁻¹). Anaesthesia and analgesia were provided with an intramuscular injection of an anaesthetic mix composed of medetomidine (0.5 mg kg⁻¹), ketamine (25 mg kg⁻¹) and buprenorphine (0.03 mg kg⁻¹). If required, anaesthesia was prolonged with further injections (half dose) of the anaesthetic mix. Eye drops were placed on the eye to prevent eye drying. The rabbit was placed on a heating pad at 35 °C for the entire procedure. Oxygen was provided with a mask to prevent hypoxia during the anaesthesia. The head was shaved and cleaned with 70% ethanol and betadine. The rabbit's head was then secured gently within a stereotactic frame (David Kopf Instruments). Before cortical skin incision, a mix of lidocaine (6 mg kg⁻¹), bupivacaine (2.5 mg kg⁻¹) and adrenaline (0.1 mg kg⁻¹) was injected subcutaneously at the surgical sites. After 5 min, the skin was opened and pulled aside to expose the skull and the skull was cleaned with cotton swabs. A temporal craniotomy was made to access the left optic nerve. The OpticSELINE was inserted in the left optic nerve from lateral to medial in the pre-chiasmatic area. The surgical implantation was performed by piercing the nerve with a needle (prolene 10-0 EH7900G, Ethicon) and by guiding the OpticSELINE transversally into the nerve with the suture until the electrode enlargement (used as a stopper). At this stage, the four alignment bars were visible on the other side of the nerve; the OpticSELINE was then slightly pulled back until only three alignment bars were visible to anchor it into the nerve. Then, a second craniotomy was made to expose the right visual cortex. A 32-channel epidural ECoG array (E32-1000-30-200; NeuroNexus) was placed on the visual cortex. All rabbits were euthanized at the end of the acute recording procedures while still under anaesthesia, with an intravenous injection of pentobarbital (120 mg kg⁻¹).

Optic-nerve anatomy. To determine the average nerve diameter, optic nerves ($n = 10$) were explanted from five female New Zealand white rabbits (>16 weeks,

>2.5 kg), immediately embedded in the optimum cutting temperature compound (Tissue-Tek, Qiagen) and frozen at -20 °C. 10 µm sections were obtained with a cryostat (Leica Microsystems) and mounted on glass slides. Images were taken with a slide scanner (VS120-L100, Olympus). For each nerve, three sections were collected and an average diameter was computed.

To determine the distribution of the fibre diameters, one female New Zealand white rabbit was perfused under anaesthesia with a mix of 2.5% glutaraldehyde and 2.0% paraformaldehyde in 0.1 M phosphate buffer (pH 7.4). The descending aorta was clamped to deliver the solution exclusively to the brain. After perfusion, the brain was left to rest for 2 h and then dissected. Both optic nerves, including the chiasm, were dissected from the skull and placed in the same fixation solution overnight at 4 °C. The tissue was then sliced transversally using a vibratome (VT1200, Leica) at a thickness of 100 µm. Slices at different positions were then washed with cacodylate buffer (0.1 M, pH 7.4), post-fixed for 40 min in 1.0% osmium tetroxide with 1.5% potassium ferrocyanide, and then for 40 min in 1.0% osmium tetroxide alone. They were finally stained for 30 min in 1% uranyl acetate in water before being dehydrated through increasing concentrations of ethanol and finally embedded in resin (Durcupan ACM, Fluka). The resin was hardened for 24 h in an oven at 65 °C. The different regions were sectioned with a diamond knife at a thickness of 0.5 µm, collected onto a glass microscope slide and stained with toluidine blue. The entire tissue section was imaged at a resolution of 92.3 nm per pixel with a transmitted-light microscope (Olympus Slide Scanner VS120-L100). The axon segmentation was performed using a customized MATLAB (MathWorks, v.R2018a) script. An image of a central section of the optic nerve was divided into 64 (8 × 8) squares, for each of which the areas of all the objects identified as axons were collected. The internal diameter of each axon was calculated assuming circularity. A histogram of the axon diameter distribution for each quadrant was created by dividing the whole range of diameters (0–3,000 nm) into bins of 50 nm width and by computing the total axon count for each bin. To normalize the height of the bars, the relative probability for each bin was computed by dividing the count of the bin by the total number of axons in the square. The median diameter of each square was used for the statistical analysis. The squares that did not contain any axons were excluded from the analysis. The axon density for each square was obtained by dividing the total number of axons by the area occupied by the axons in that square.

Electrophysiology. For optic-nerve stimulation, the OpticSELINE was attached to a current stimulator (IZ2MH; Tucker-Davis Technologies), whereas for cortical recordings, the ECoG array (E32-1000-30-200; NeuroNexus) was connected to an amplifier (PZ5; Tucker-Davis Technologies) via a 32-channel analogue head stage (ZIF-Clip Analog Headstage; Tucker-Davis Technologies). Optic-nerve stimulation was performed with 13 pulse amplitudes (10, 25, 50, 75, 100, 150, 200, 250, 500, 750, 1,000, 1,500 and 2,000 µA) and 5 pulse durations (50, 100, 150, 200 and 400 µs) delivered in a scrambled manner. Data were filtered between 0.5 Hz and 2 kHz and digitized at 12 kHz. Epochs (from -100 to 750 ms) synchronous to the onset of the stimulation were then extracted from the data stream and data analysis was performed with MATLAB.

Blind source separation. For each recording electrode and each stimulation intensity, epochs were concatenated and processed with an AMICA³⁷ core and GPU-processed infomax reliable ICA (RELICA) algorithm³⁸. Dimensionality reduction on the data as a pre-processing step to ICA was not performed³⁹. RELICA allowed us to test the repeatability of ICs appearing in decompositions of bootstrapped versions of the input data and to retain only stable ICs for further analysis. Given the multivariate dataset from the 32 recording electrodes X (electrode, time), ICA extracts an unmixing matrix W (32 × 32) such that the IC time courses $S = WX$ are maximally independent. Rows of W represent the weights applied to each electrode to obtain the corresponding ICs S . The i^{th} column of the mixing matrix A (pseudoinverse of W) represents the weight of the i^{th} IC on each recording electrode and can be represented as an activation map. Each activation map was obtained by projecting the weights of the unmixing matrix A onto the layout of the ECoG array, then by spatially interpolating them with a spline function, and finally by normalizing the maps to the maximal absolute value present in the interpolated map. IC grand-average time courses, obtained by performing the average over trials for each stimulation intensity, formed the IC-EEPs. The PVAF by each IC on each electrode was computed and represented as a PVAF activation map. ICs were categorized into several classes: flat, common, artefact, noise and meaningful (Supplementary Fig. 6a). First, low-frequency components of the signal were removed using a zero-phase high-pass filter with a 5 Hz cut-off frequency. Then, artefact ICs, exhibiting a large activation within the first 5 ms from the stimulus onset, were identified by visual inspection and removed. To verify that the artefact ICs were correctly identified, all the other ICs were back-projected. The initial portion of the back-projected signal (0 to 5 ms) was indeed exclusively affected by the manual removal of the artefact ICs when compared to the original signal (Supplementary Fig. 10). Following the identification of the artefact, the noise ICs were identified by computing the frequency plot of the signal; the ICs exhibiting unusual peaks in the 250 to 500 Hz frequency range were labelled noise (Supplementary Fig. 6b). Among the remaining ICs (Supplementary Fig. 6c), the ones with a peak-to-peak variation

(Δ) in the time course (time frame from 5 to 25 ms after the stimulus) smaller than three times the standard deviation of the time course (σ) were labelled as flat ($\Delta/\sigma < 3$). To separate meaningful ICs from common ICs, a similarity index was used: that is, the correlation between the time courses of the different stimulating electrodes. ICs were classified as common (that is, with visible meaningful activation but with similar time courses for all the stimulating electrodes) when exhibiting a mean similarity index larger than 0.5. The distribution maps in the optic nerve were obtained by interpolating the contribution of every stimulating electrode to each IC with a spline function. The contour of the optic nerve was set to zero. Meaningful ICs were further classified into meaningful clusters by grouping together the ICs that were associated with similar portions of the optic nerve. We defined a similarity index consisting of the average area overlap between the 90% area of the distribution maps at the level of the optic nerve of each pair of meaningful ICs. A perfect overlap between the 90% area is a score of one and no overlap is a score of zero. On the basis of this similarity, we used the complete-linkage clustering method to build a clustering tree of the meaningful ICs. ICs that had at least 50% overlap were clustered.

Hybrid FEA model and NEURON simulation. A realistic electrical and structural model was built by combining a three-dimensional FEA model in COMSOL Multiphysics (v.5.2.262) to determine the electrical potential distribution inside the optic nerve with a biophysical-cable model of the optic-nerve axons simulated in the NEURON environment (v.7.4). The FEA model was built using COMSOL's stationary-current study with the AC/DC module. The optic-nerve model consists of a central cylinder surrounded by the meningeal layers, modelled as concentric cylinders. In particular, the pia mater was approximated by a contact impedance due to its very small thickness, and the cerebrospinal fluid was placed between the pia mater and the dura mater. The optic nerve is surrounded by a volume of saline solution. The OpticSELINE is inserted transversely through the centre of the optic-nerve domain so that each of the four central electrodes, modelled as boundary current sources of 0.008 mm², is equidistant from the centre of the optic-nerve domain. Finally, a large return electrode is modelled in saline medium. Except for the optic-nerve domain, which has a larger electrical conductivity along its axis, all the other domains have isotropic conductivity. The size (in μm) and conductivity (in S m^{-1}) of the different domains are as follows. For the optic nerve, the radius is 750, the longitudinal electrical conductivity is 0.5 and the transversal electrical conductivity is 0.08 (ref. ⁶⁰). For the pia mater, the thickness is 10 and the electrical conductivity is 0.016 (ref. ⁶⁰). For the dura mater, the thickness is 300 and the electrical conductivity is 0.06 (ref. ⁶¹). For the cerebrospinal fluid, the thickness is 100 and the electrical conductivity is 1.7 (ref. ⁶²). For the saline, the electrical conductivity is 1.7 (ref. ⁶²).

A monophasic unitary current pulse was injected through one of the electrodes while the current in the others was set to zero. Quasi-static approximation of Maxwell equations is valid at the frequency range of the experiment⁶³. Therefore, the extracellular electrical potential V_e resulting from the injection of the current can be computed with the Laplace formulation: equation (1)⁶⁴:

$$\nabla \cdot \sigma \nabla V_e = 0 \quad (1)$$

Resulting in equation (2), with the Dirichlet boundary conditions set to zero at the external part of the box:

$$V_e(\delta\Omega) = 0 \quad (2)$$

where $\delta\Omega$ represents the basis of the cylinders and the outer surface of the saline box.

The size of the saline box and the mesh size were optimized to respect the hypothesis of ground condition at infinity. We tested models with different combinations of length and radius of the saline box, all of which had a mesh composed of tetradic second-order elements. To achieve better accuracy, the mesh close to the electrode, where the steeper change in the electrical potential occurs, was made finer by making two concentric spheres of smaller mesh size around the electrode. According to frequently used indexes in FEA⁶⁵, we optimized the size of the saline box as 4.5 mm in diameter and a total length of 5 mm.

The axon-fibre models were implemented in NEURON as McNeal's cable model; only the nodes of Ranvier are active segments, while the myelinated segments are approximated by a perfect insulator. The geometric parameters used to build each axon model were obtained from a previous work⁴⁴. Each axon model is a modified Hodgkin–Huxley model⁶⁶, with each of its nodes of Ranvier containing five types of currents: fast sodium current, fast potassium current, persistent sodium current, slow potassium current and leak current. The electrical properties of the axon were obtained from a previous work⁴⁷. The axon models allow determination of whether a set of extracellular-potential values (obtained from the interpolation of the potential distribution from the FEA model at the locations of their nodes of Ranvier) can generate an action potential. An axon is defined as activated if an action potential travels to both of its ends. For an axon of a given diameter and shift (the relative distance separating its central node of Ranvier from the centre of the stimulating electrode), its probability of being activated by the stimulation is binary: either 0 or 1. To determine the probability of a certain pair of coordinates in the optic-nerve cross-section containing an

axon activated by a given electrical stimulation, the probabilities of all possible axons passing were computed. We tested a total of 60 combinations of diameters and shifts: 12 diameters ranging from 0.25 to 3 μm and 6 shifts (ranging from 0 if the electrode is aligned with the central node of Ranvier to 0.5 if the electrode aligned with the centre of the myelinated segment, with an interval of 0.1). Each of these 60 probabilities was weighted by a factor that consists of the frequency of occurrence of the diameter it corresponds to, multiplied by the squared diameter of the axons. Once weighted, these probabilities were summed to give the final combined probability of activation. We sampled the probability of activation at every 40 $\mu\text{m} \times 40 \mu\text{m}$ pair of coordinates over the entire cross-section of the optic nerve and re-sampled it more finely at the locations where an important change in the probability of activation was present. These probabilities of activation were linearly interpolated to give the final probability maps with a resolution of 1 μm .

Statistical analysis and graphical representation. Statistical analysis and graphical representation were performed with Prism (GraphPad Software, v.8.1.2). The normality test (D'Agostino and Pearson omnibus-normality test) was performed in each dataset to justify the use of a parametric or non-parametric test. In each figure, P -values are represented as * $P < 0.05$, ** $P < 0.01$, *** $P < 0.001$ and **** $P < 0.0001$. Data are reported as the mean \pm s.e.m. or mean \pm s.d.; n is used to identify the number of electrodes, trials or nerves; N is used to identify the number of rabbits.

Reporting summary. Further information on research design is available in the Nature Research Reporting Summary linked to this article.

Data availability

The authors declare that all data supporting the results in this study are available within the paper and its Supplementary Information. The raw and analysed datasets generated during the study are available for research purposes from the corresponding author on reasonable request.

Code availability

Code used for the hybrid FEA model and NEURON simulation is available at <https://github.com/Ine-lab/nBME2019>. The authors declare that the algorithm used for blind source separation is described in the referenced papers. The source code can be obtained from S.M. (silvestro.micera@epfl.ch) upon reasonable request.

Received: 25 April 2018; Accepted: 18 July 2019;

Published online: 19 August 2019

References

- Bourne, R. R. et al. Causes of vision loss worldwide, 1990–2010: a systematic analysis. *Lancet Glob. Health* **1**, e339–e349 (2013).
- Brindley, G. & Lewin, W. The sensations produced by electrical stimulation of the visual cortex. *J. Physiol.* **196**, 479–493 (1968).
- Dobelle, W., Mladejovsky, M. & Girvin, J. Artificial vision for the blind: Electrical stimulation of visual cortex offers hope for a functional prosthesis. *Science* **183**, 440–444 (1974).
- Zrenner, E. Fighting blindness with microelectronics. *Sci. Transl. Med.* **5**, 210ps16 (2013).
- Ghezzi, D. Retinal prostheses: progress toward the next generation implants. *Front. Neurosci.* **9**, 290 (2015).
- Stingl, K. et al. Artificial vision with wirelessly powered subretinal electronic implant alpha-IMS. *Proc. R. Soc. B* **280**, 20130077 (2013).
- da Cruz, L. et al. Five-year safety and performance results from the Argus II retinal prosthesis system clinical trial. *Ophthalmology* **123**, 2248–2254 (2016).
- Ayton, L. N. et al. First-in-human trial of a novel suprachoroidal retinal prosthesis. *PLoS ONE* **9**, e115239 (2014).
- Brelén, M. E., Vince, V., Gérard, B., Veraart, C. & Delbeke, J. Measurement of evoked potentials after electrical stimulation of the human optic nerve. *Invest. Ophthalmol. Vis. Sci.* **51**, 5351–5355 (2010).
- Panetsos, F., Sanchez-Jimenez, A., Cerio, E., Diaz-Guemes, I. & Sanchez, F. M. Consistent phosphenes generated by electrical microstimulation of the visual thalamus. An experimental approach for thalamic visual neuroprostheses. *Front. Neurosci.* **5**, 84 (2011).
- Normann, R. A. et al. Toward the development of a cortically based visual neuroprosthesis. *J. Neural Eng.* **6**, 035001 (2009).
- Merabet, L. B., Rizzo, J. F., Amedi, A., Somers, D. C. & Pascual-Leone, A. What blindness can tell us about seeing again: merging neuroplasticity and neuroprostheses. *Nat. Rev. Neurosci.* **6**, 71–77 (2005).
- Luo, Y. & da Cruz, L. The Argus II retinal prosthesis system. *Prog. Retin. Eye Res.* **50**, 89–107 (2016).
- Stingl, K. et al. Subretinal visual implant Alpha IMS—Clinical trial interim report. *Vis. Res.* **111**, 149–160 (2015).
- Lorach, H. et al. Photovoltaic restoration of sight with high visual acuity. *Nat. Med.* **21**, 476–482 (2015).

16. Ferlauto, L. et al. Design and validation of a foldable and photovoltaic wide-field epiretinal prosthesis. *Nat. Commun.* **9**, 992 (2018).
17. Antognazza, M. et al. Shedding light on living cells. *Adv. Mater.* **27**, 7662–7669 (2015).
18. Maya-Vetencourt, J. et al. A fully organic retinal prosthesis restores vision in a rat model of degenerative blindness. *Nat. Mater.* **16**, 681–689 (2017).
19. Antognazza, M. et al. Characterization of a polymer-based, fully organic prosthesis for implantation into the subretinal space of the rat. *Adv. Health. Mater.* **5**, 2271–2282 (2016).
20. Veraart, C. et al. Visual sensations produced by optic nerve stimulation using an implanted self-sizing spiral cuff electrode. *Brain Res.* **813**, 181–186 (1998).
21. Brelén, M. E. et al. Intraorbital implantation of a stimulating electrode for an optic nerve visual prosthesis. *J. Neurosurg.* **104**, 593–597 (2006).
22. Duret, F. et al. Object localization, discrimination, and grasping with the optic nerve visual prosthesis. *Restor. Neurol. Neurosci.* **24**, 31–40 (2006).
23. Veraart, C., Wanet-Defalque, M., Gérard, B., Vanlierde, A. & Delbeke, J. Pattern recognition with the optic nerve visual prosthesis. *Artif. Organs* **27**, 996–1004 (2003).
24. Brelén, M., Duret, F., Gérard, B., Delbeke, J. & Veraart, C. Creating a meaningful visual perception in blind volunteers by optic nerve stimulation. *J. Neural Eng.* **2**, S22 (2005).
25. The Lasker/IRRF Initiative for Innovation in Vision Science. Chapter 1 – Restoring vision to the blind: The new age of implanted visual prostheses. *Transl. Vis. Sci. Technol.* <https://doi.org/10.1167/tvst.3.7.3> (2014).
26. Yan, Y. et al. Electrically evoked responses in the rabbit cortex induced by current steering with penetrating optic nerve electrodes. *Invest. Ophthalmol. Vis. Sci.* **57**, 6327–6338 (2016).
27. Sun, J., Chen, Y., Chai, X., Ren, Q. & Li, L. Penetrating electrode stimulation of the rabbit optic nerve: parameters and effects on evoked cortical potentials. *Graefes Arch. Clin. Exp. Ophthalmol.* **251**, 2545–2554 (2013).
28. Lu, Y. et al. Electrical stimulation with a penetrating optic nerve electrode array elicits visuotopic cortical responses in cats. *J. Neural Eng.* **10**, 036022 (2013).
29. Raspopovic, S. et al. Restoring natural sensory feedback in real-time bidirectional hand prostheses. *Sci. Transl. Med.* **6**, 222ra19–222ra19 (2014).
30. Oddo, C. et al. Intraneural stimulation elicits discrimination of textural features by artificial fingertip in intact and amputee humans. *eLife* **5**, e09148 (2016).
31. Raspopovic, S., Capogrosso, M., Badia, J., Navarro, X. & Micera, S. Experimental validation of a hybrid computational model for selective stimulation using transverse intrafascicular multichannel electrodes. *IEEE Trans. Neural Syst. Rehabil. Eng.* **20**, 395–404 (2012).
32. Badia, J. et al. Comparative analysis of transverse intrafascicular multichannel, longitudinal intrafascicular and multipolar cuff electrodes for the selective stimulation of nerve fascicles. *J. Neural Eng.* **8**, 036023 (2011).
33. Cutrone, A. et al. A three-dimensional self-opening intraneural peripheral interface (SELINE). *J. Neural Eng.* **12**, 016016 (2015).
34. Wurth, S. et al. Long-term usability and bio-integration of polyimide-based intra-neural stimulating electrodes. *Biomaterials* **122**, 114–129 (2017).
35. Hukins, D. W. L., Mahomed, A. & Kukureka, S. N. Accelerated aging for testing polymeric biomaterials and medical devices. *Med. Eng. Phys.* **30**, 1270–1274 (2008).
36. Howlader, M., Doyle, T., Mohtashami, S. & Kish, J. Charge transfer and stability of implantable electrodes on flexible substrate. *Sens. Actuators B Chem.* **178**, 132–139 (2013).
37. Giolli, R. & Guthrie The primary optic projections in the rabbit. An experimental degeneration study. *J. Comp. Neurol.* **136**, 99–126 (1969).
38. Sun, J. et al. Spatiotemporal properties of multi-peaked electrically evoked potentials elicited by penetrative optic nerve stimulation in rabbits. *Invest. Ophthalmol. Vis. Sci.* **52**, 146–154 (2011).
39. Delorme, A., Palmer, J., Onton, J., Oostenveld, R. & Makeig, S. Independent EEG sources are dipolar. *PLoS ONE* **7**, e30135 (2012).
40. Menicucci, D. et al. Brain responses to emotional stimuli during breath holding and hypoxia: an approach based on the independent component analysis. *Brain Topogr.* **27**, 771–785 (2014).
41. Artoni, F. et al. Unidirectional brain to muscle connectivity reveals motor cortex control of leg muscles during stereotyped walking. *NeuroImage* **159**, 403–416 (2017).
42. Bell, A. & Sejnowski, T. An information-maximization approach to blind separation and blind deconvolution. *Neural Comput.* **7**, 1129–1159 (1995).
43. Delbeke, J., Oozeer, M. & Veraart, C. Position, size and luminosity of phosphores generated by direct optic nerve stimulation. *Vis. Res.* **43**, 1091–1102 (2003).
44. Li, M. et al. A simulation of current focusing and steering with penetrating optic nerve electrodes. *J. Neural Eng.* **10**, 066007 (2013).
45. Ghezzi, D. et al. A polymer optoelectronic interface restores light sensitivity in blind rat retinas. *Nat. Photonics* **7**, 400–406 (2013).
46. Mathieson, K. et al. Photovoltaic retinal prosthesis with high pixel density. *Nat. Photonics* **6**, 391–397 (2012).
47. Mandel, Y. et al. Cortical responses elicited by photovoltaic subretinal prostheses exhibit similarities to visually evoked potentials. *Nat. Commun.* **4**, 1980 (2013).
48. Tang, J. et al. Nanowire arrays restore vision in blind mice. *Nat. Commun.* **9**, 786 (2018).
49. Sakaguchi, H. et al. Artificial vision by direct optic nerve electrode (AV-DONE) implantation in a blind patient with retinitis pigmentosa. *J. Artif. Organs* **12**, 206–209 (2009).
50. Boinagrov, D., Pangratz-Fuehrer, S., Goetz, G. & Palanker, D. Selectivity of direct and network-mediated stimulation of the retinal ganglion cells with epi-, sub- and intraretinal electrodes. *J. Neural Eng.* **11**, 026008 (2014).
51. Weiland, J. D., Walston, S. T. & Humayun, M. S. Electrical stimulation of the retina to produce artificial vision. *Annu. Rev. Vis. Sci.* **2**, 273–294 (2016).
52. Nirenberg, S. & Pandarinath, C. Retinal prosthetic strategy with the capacity to restore normal vision. *Proc. Natl Acad. Sci. USA* **109**, 15012–15017 (2012).
53. Piedade, M., Gerald, J., Sousa, L., Tavares, G. & Tomás, P. Visual neuroprosthesis: a non invasive system for stimulating the cortex. *IEEE Trans. Circuits Syst. I* **52**, 2648–2662 (2005).
54. Sieu, L.-A. A. et al. EEG and functional ultrasound imaging in mobile rats. *Nat. Methods* **12**, 831–834 (2015).
55. Demene, C. et al. Functional ultrasound imaging of brain activity in human newborns. *Sci. Transl. Med.* **9**, eaah6756 (2017).
56. Blaize, K. et al. Functional ultrasound imaging of deep visual cortex in awake non-human primates. Preprint at *Biorxiv* <https://doi.org/10.1101/551663> (2019).
57. Palmer, J. A., Kreutz-Delgado, K., Rao, B. D. & Makeig, S. in *Independent Component Analysis and Signal Separation* (eds Davies M.E. et al.) 90–97 (Springer, 2007).
58. Artoni, F., Menicucci, D., Delorme, A., Makeig, S. & Micera, S. RELICA: a method for estimating the reliability of independent components. *NeuroImage* **103**, 391–400 (2014).
59. Artoni, F., Delorme, A. & Makeig, S. Applying dimension reduction to EEG data by principal component analysis reduces the quality of its subsequent independent component decomposition. *NeuroImage* **175**, 176–187 (2018).
60. Goodall, E. V., Kosterman, L. M., Holsheimer, J. & Struijk, J. J. Modeling study of activation and propagation delays during stimulation of peripheral nerve fibers with a tripolar cuff electrode. *IEEE Trans. Rehabil. Eng.* **3**, 272–282 (1995).
61. Chintalacharuvu, R. R., Ksienski, D. A. & Mortimer, J. T. A numerical analysis of the electric field generated by a nerve cuff electrode. *Proc. Annual International Conference of the IEEE Engineering in Medicine and Biology Society* 912–913 (IEEE, 1991).
62. Struijk, J. J., Holsheimer, J., Barolat, G., He, J. & Boom, H. B. K. Paresthesia thresholds in spinal cord stimulation: a comparison of theoretical results with clinical data. *IEEE Trans. Rehabil. Eng.* **1**, 101–108 (1993).
63. Bossetti, C. A., Birdno, M. J. & Grill, W. M. Analysis of the quasi-static approximation for calculating potentials generated by neural stimulation. *J. Neural Eng.* **5**, 44 (2008).
64. McIntyre, C. C. & Grill, W. M. Extracellular stimulation of central neurons: influence of stimulus waveform and frequency on neuronal output. *J. Neurophysiol.* **88**, 1592–1604 (2002).
65. Raspopovic, S., Capogrosso, M. & Micera, S. A computational model for the stimulation of rat sciatic nerve using a transverse intrafascicular multichannel electrode. *IEEE Trans. Neural Syst. Rehabil. Eng.* **19**, 333–344 (2011).
66. Hodgkin, A. & Huxley, A. A quantitative description of membrane current and its application to conduction and excitation in nerve. *J. Physiol.* **117**, 500–544 (1952).
67. Oozeer, M., Veraart, C., Legat, V. & Delbeke, J. A model of the mammalian optic nerve fibre based on experimental data. *Vis. Res.* **46**, 2513–2524 (2006).

Acknowledgements

We acknowledge the support from the Bioelectron Microscopy Core Facility (BIOEM) of Ecole polytechnique fédérale de Lausanne. This work has been supported by Ecole polytechnique fédérale de Lausanne, Medtronic, Bertarelli Foundation and Wyss Center for Bio and Neuroengineering. F.A. is supported by the European Union's Horizon 2020 research and innovation programme under Marie Skłodowska-Curie Action agreement no. 750947 (BIREHAB).

Author contributions

V.G. designed the stimulation protocol and performed the modelling and simulation, blind source separation and data analysis. A.C. designed and fabricated the OpticSELINE and performed mechanical and electrochemical characterizations. F.A. conceived and performed the blind source separation approach. P.V. performed in vivo and histological

experiments. A.M.P. performed the modelling and simulation. S.A.R. participated in the design of the stimulation protocol and data analysis. D.L.D.P. participated in the design and microfabrication of the OpticSELINE and performed mechanical characterizations. S.M. supervised the activities related to electrode development and the blind source separation approach. D.G. designed the study, led the project and wrote the manuscript. All the authors read, edited, and accepted the manuscript.

Competing interests

The authors declare no competing interests.

Additional information

Supplementary information is available for this paper at <https://doi.org/10.1038/s41551-019-0446-8>.

Reprints and permissions information is available at www.nature.com/reprints.

Correspondence and requests for materials should be addressed to D.G.

Publisher's note: Springer Nature remains neutral with regard to jurisdictional claims in published maps and institutional affiliations.

© The Author(s), under exclusive licence to Springer Nature Limited 2019

Reporting Summary

Nature Research wishes to improve the reproducibility of the work that we publish. This form provides structure for consistency and transparency in reporting. For further information on Nature Research policies, see [Authors & Referees](#) and the [Editorial Policy Checklist](#).

Statistics

For all statistical analyses, confirm that the following items are present in the figure legend, table legend, main text, or Methods section.

n/a Confirmed

- | | | |
|-------------------------------------|-------------------------------------|--|
| <input type="checkbox"/> | <input checked="" type="checkbox"/> | The exact sample size (<i>n</i>) for each experimental group/condition, given as a discrete number and unit of measurement |
| <input type="checkbox"/> | <input checked="" type="checkbox"/> | A statement on whether measurements were taken from distinct samples or whether the same sample was measured repeatedly |
| <input type="checkbox"/> | <input checked="" type="checkbox"/> | The statistical test(s) used AND whether they are one- or two-sided
<i>Only common tests should be described solely by name; describe more complex techniques in the Methods section.</i> |
| <input checked="" type="checkbox"/> | <input type="checkbox"/> | A description of all covariates tested |
| <input type="checkbox"/> | <input checked="" type="checkbox"/> | A description of any assumptions or corrections, such as tests of normality and adjustment for multiple comparisons |
| <input type="checkbox"/> | <input checked="" type="checkbox"/> | A full description of the statistical parameters including central tendency (e.g. means) or other basic estimates (e.g. regression coefficient) AND variation (e.g. standard deviation) or associated estimates of uncertainty (e.g. confidence intervals) |
| <input type="checkbox"/> | <input checked="" type="checkbox"/> | For null hypothesis testing, the test statistic (e.g. <i>F</i> , <i>t</i> , <i>r</i>) with confidence intervals, effect sizes, degrees of freedom and <i>P</i> value noted
<i>Give P values as exact values whenever suitable.</i> |
| <input checked="" type="checkbox"/> | <input type="checkbox"/> | For Bayesian analysis, information on the choice of priors and Markov chain Monte Carlo settings |
| <input checked="" type="checkbox"/> | <input type="checkbox"/> | For hierarchical and complex designs, identification of the appropriate level for tests and full reporting of outcomes |
| <input checked="" type="checkbox"/> | <input type="checkbox"/> | Estimates of effect sizes (e.g. Cohen's <i>d</i> , Pearson's <i>r</i>), indicating how they were calculated |

Our web collection on [statistics for biologists](#) contains articles on many of the points above.

Software and code

Policy information about [availability of computer code](#)

Data collection

For electrophysiological data collection, we used the proprietary software 'Synapse' from TUCKER-DAVIS TECHNOLOGIES.

Data analysis

Data analysis has been performed using the following software: MATLAB (Version R2018a), COMSOL Multiphysics (Version 5.2.262), NEURON (Version 7.4), Prism (Version 8.1.2).
For blind source separation an AMICA core (10.1007/978-3-540-74494-8_13) and GPU-processed infomax reliable ICA (RELICA) algorithm (10.1016/j.neuroimage.2014.09.010) were used.

For manuscripts utilizing custom algorithms or software that are central to the research but not yet described in published literature, software must be made available to editors/reviewers. We strongly encourage code deposition in a community repository (e.g. GitHub). See the Nature Research [guidelines for submitting code & software](#) for further information.

Data

Policy information about [availability of data](#)

All manuscripts must include a [data availability statement](#). This statement should provide the following information, where applicable:

- Accession codes, unique identifiers, or web links for publicly available datasets
- A list of figures that have associated raw data
- A description of any restrictions on data availability

The authors declare that all data supporting the results in this study are available within the paper and its Supplementary Information. The raw and analysed datasets generated during the study are available for research purposes from the corresponding authors on reasonable request.

Field-specific reporting

Please select the one below that is the best fit for your research. If you are not sure, read the appropriate sections before making your selection.

☒ Life sciences ☐ Behavioural & social sciences ☐ Ecological, evolutionary & environmental sciences

For a reference copy of the document with all sections, see [nature.com/documents/nr-reporting-summary-flat.pdf](https://www.nature.com/documents/nr-reporting-summary-flat.pdf)

Life sciences study design

All studies must disclose on these points even when the disclosure is negative.

Sample size	This paper does not include any allocation to experimental groups. Sample size was thus not determined with a statistical test.
Data exclusions	No data were excluded from the analyses.
Replication	All attempts to replicate the data were successful. Experiments were reproduced at least 4 times (as stated in the main text). Only the experiment in Supplementary Figure 5 was repeated once.
Randomization	This paper does not include any allocation to experimental groups. Therefore, randomization is not relevant in the context of this study.
Blinding	As per the point above, blinding does not apply.

Reporting for specific materials, systems and methods

We require information from authors about some types of materials, experimental systems and methods used in many studies. Here, indicate whether each material, system or method listed is relevant to your study. If you are not sure if a list item applies to your research, read the appropriate section before selecting a response.

Materials & experimental systems

n/a	Involved in the study
<input checked="" type="checkbox"/>	<input type="checkbox"/> Antibodies
<input checked="" type="checkbox"/>	<input type="checkbox"/> Eukaryotic cell lines
<input checked="" type="checkbox"/>	<input type="checkbox"/> Palaeontology
<input type="checkbox"/>	<input checked="" type="checkbox"/> Animals and other organisms
<input checked="" type="checkbox"/>	<input type="checkbox"/> Human research participants
<input checked="" type="checkbox"/>	<input type="checkbox"/> Clinical data

Methods

n/a	Involved in the study
<input checked="" type="checkbox"/>	<input type="checkbox"/> ChIP-seq
<input checked="" type="checkbox"/>	<input type="checkbox"/> Flow cytometry
<input checked="" type="checkbox"/>	<input type="checkbox"/> MRI-based neuroimaging

Animals and other organisms

Policy information about [studies involving animals](#); [ARRIVE guidelines](#) recommended for reporting animal research

Laboratory animals	Female New Zealand White rabbits (> 16 weeks, > 2.5 kg).
Wild animals	The study did not involve wild animals.
Field-collected samples	The study did not involve samples collected from the field.
Ethics oversight	Animal experiments were performed under the authorization GE1416, approved by the Département de l'emploi, des affaires sociales et de la santé (DEAS), Direction générale de la santé of the République et Canton de Genève (Switzerland).

Note that full information on the approval of the study protocol must also be provided in the manuscript.